

## Review article

## Bentheimer sandstone revisited for experimental purposes



Anna E. Peksa\*, Karl-Heinz A.A. Wolf, Pacelli L.J. Zitha

Delft University of Technology, Department of Geotechnology, Stevinweg 1, 2628 CN Delft, The Netherlands

## ARTICLE INFO

## Article history:

Received 8 January 2015

Received in revised form

23 April 2015

Accepted 3 June 2015

Available online 11 June 2015

## Keywords:

Bentheimer sandstone

Mineralogy

Porosity

Permeability

Grain/pore-size

Dielectric behavior

## ABSTRACT

Bentheimer sandstone outcrop samples are ideal for laboratory studies due to their lateral continuity and block scale homogeneous nature. Over the years they have been used to investigate reservoir topics ranging from passive and active properties of oil/gas/water/rock interaction and processes to flow and transport.

This work shows an evaluation of Bentheimer sandstone properties and their characteristics to advance understanding on the mineral accessory and the physical and electrical transport properties. On the basis of the nature of depositional environments and diagenesis, we measure and characterize spatial attributes of the matrix, mainly by qualitative analysis, laboratory and stereological measurements and statistical 2D/3D reconstructions. The main contribution of this paper is the impact of mineral composition on the petrophysical quality and block scale homogeneity of the reservoir. With 3D techniques reconstructions of the new rock grain framework pore structures have been created.

Based on measurements, a review of literature data and interpretation of variation between the outcrops and flow relevant parameters, we conclude that Bentheimer sandstone is a rock that shows constant mineralogy and is largely free of paramagnetic impurities. In accordance with the results of 3D reconstructions techniques and in line with the depositional settings, they show a well sorted grain framework and a pore network that can be used to calculate the permeability and resistivity without conducting any direct laboratory measurements of either parameter. It presents a porosity with a range of 0.21–0.27 and permeabilities varying between 0.52 and 3.02 Darcy. Based on our work and literature, it is found that high permeability together with similar distribution of pore throats and bodies make the sandstone an attractive and easy obtainable candidate for comparative experimental studies. Moreover, we state by comparing various techniques that the efficiency and resolution accuracy of the applied method must be taken into consideration when planning the measurements.

© 2015 Elsevier Ltd. All rights reserved.

## 1. Introduction

Bentheimer sandstone (BS) is a shallow marine formation deposited during the Lower Cretaceous. It forms a reservoir for oil and on the border between the Netherlands and Germany, outcropping in Bentheim with shallow oil reservoirs in between Enschede and Schoonenbeek (Dubelaar and Nijland, 2015; Fuchtbauer, 1963; Fuchtbauer, 1955; Kemper, 1968, 1976; Knaap and Coenen, 1987). The sandstone is considered to be an ideal sedimentary rock for reservoir studies due to its lateral continuity and homogeneous block-scale nature. Both in natural appearance and thermally treated, it has a limited amount of minerals, a constant grain size distribution, porosity, permeability and dielectrical

values, which makes it suitable for standard laboratory experiments and associated comparison with theory (Klein and Reuschlé, 2003; Ruedrich and Siegesmund, 2007). Therefore, Bentheimer sandstone is used to investigate a variety of reservoir topics ranging from passive and active properties of oil recovery processes to flow and transport in the groundwater zone and environmental remediation. Also, researchers often use Bentheimer sandstone in energy production studies and related processes such as geothermal energy (Jacquey et al., 2014a, 2014b; Reyer and Philipp, 2014; Smith and McKibbin, 2000) and geological storage of carbon dioxide (Al-Mehali et al., 2014; Andersson et al., 2013; Andrew et al., 2013a; Herring, 2012; Holt et al., 1995; Kvamme et al., 2006; Shojaikaveh et al., 2012).

The homogeneity and isotropy of rocks have a strong relation to the propagation of underground fluids. The major characteristics that are responsible for sandstone's homogeneity and isotropy at

\* Corresponding author.

E-mail address: [A.E.Peksa@tudelft.nl](mailto:A.E.Peksa@tudelft.nl) (A.E. Peksa).

<b>Nomenclature</b>			
A	Area, m <sup>2</sup>	rw	Residual water
C	Constant associated with the tortuosity, [-]	s	Surface
D	Diameter, mm	sol	Dissolution
$\Delta n$	Dissolution rate, mmol	st	Standard
E	Young's modulus, GPa	t	Tangent
F	Faraday constant, C/mol	v	Vapor
$\gamma$	Surface tension of the liquid surface, J/m <sup>2</sup>	w	Water
K	Permeability, D		
$K_o$	Kozeny constant, [-]		
L	Height, mm		
$L_e/L$	Tortuosity, where $L_e$ is the effective length and L the curved length, [-]		
M	Mass, g		
$\nu$	Poisson's ratio, [-]		
p	Pressure, Pa		
P	Perimeter, mm		
$\varphi$	Effective porosity, [-]		
r	Radii of curvature, m		
R	Ideal gas constant, J/K mol		
$\rho$	Bulk density, kg/m <sup>3</sup>		
S	Saturation [-]		
$S_s$	Specific surface, m/m <sup>2</sup>		
$\delta$	Charge, C/m <sup>2</sup>		
$\sigma$	Stress, MPa		
T	Temperature, K		
V	Volume, m <sup>3</sup>		
<i>Subscripts</i>			
a	Area		
ave	Average		
b	Pore body		
g	Grain		
max	Maximum		
m	Molar		
p	Pore		
		<i>Abbreviations</i>	
		ASTM	American Society for Testing and Materials Standard Documents (+reference code)
		BET	Brunauer–Emmett–Teller
		BS	Bentheimer sandstone
		CO <sub>2</sub>	Carbon dioxide
		CT	Computed tomography
		FS	Fresh core samples
		FSQ	Fresh core samples collected at different locations of the Romberg Quarry
		GM	Gravimetric method
		H <sup>+</sup>	Hydrogen ion
		H <sub>2</sub> O	Water
		HCl	Hydrogen chloride
		IS	Intermediate core samples
		Max	Maximum
		$\mu$ CT	Micro-CT scanner
		N <sub>2</sub>	Nitrogen
		NaCl	Sodium chloride
		NaOH	Sodium hydroxide
		OS	Old core samples
		PZC	Point of zero charge
		SEM	Scanning Electron Microscope
		STD	Standard deviation
		STP	Standard Test Procedure
		TS	Thin section
		UP	Ultra Pycnometer
		XRD	X-ray Diffraction
		XRF	X-ray Fluorescence

the small scale relate to grain size distribution, the orientation of the mineral grains/pores along a preferential direction (Wright et al., 2006), porosity and permeability – and even for samples obtained from different locations, the lack of mineral dissolution and precipitation processes that may increase the anisotropy and effectively decrease the connectivity. At field scale the homogeneity of the reservoir is predominantly determined by layering (Chandler et al., 1989), the existence of clay minerals in the zones of shear (Clavaud et al., 2008), and preferred alignment of fractures and faults.

In this study we describe the degree of block-scale homogeneity of the sample for conventional experiments and, for the more recent types of experiments (i.e., wettability and electrokinetic studies). Thus, our motivation is an unprecedented conduction, analysis and collection from the literature the prenominal Bentheimer sandstone parameters. Knowing depositional environments and diagenesis, we measure and characterize spatial attributes of the matrix, mainly by qualitative analysis, laboratory and stereological measurements and statistical 2D/3D reconstructions. In addition, we focus on overcoming the shortcomings in the literature (i.e., determination of the grain size distribution with a use of micro-CT scanner, the surface charge profile of Bentheimer sandstone with emphasis on the role of hematite and goethite).

This study was conducted at three different scales: (1) site scale (outcrop investigation); (2) laboratory scale (standard core testing); (3) microscopic scale (optical microscope, electron scanning environmental microscope), and calculated micro-scale (micro-CT and medical-CT scanner). In addition, the dielectrical behavior of the sandstone is considered as a measure for the definition of impurities in the quartz rich sandstone. This information is important for instance in wettability studies for CO<sub>2</sub> storage.

This research starts with the introduction of geological settings, variations on the environmental interpretations between the outcrops, and where possible, flow relevant parameters. Here primarily core measurements are considered, as they provide input data to classical reservoir evaluations and possible spread in data. The ability to predict the permeability of a porous medium and understand the impact of the pore structure is therefore imperative. Uncertainties in macroscopic reservoir characterization may originate from uncertainties in core data and consequently a more detailed microstructure characterization of Bentheimer sandstone was performed. The microstructure has a significant effect on bulk physical properties such as permeability, mechanical behavior (elastic moduli, relaxation times), electrical conductivity and heat capacity. For that reason we conducted XRD and XRF analysis and gathered the data from various studies (to make a comparison of mineral composition and amounts) (Al-Muntasher et al., 2010;

Kemper, 1968, 1976; Maloney et al., 1990; Mayr and Burkhardt, 2006; Van Baaren et al., 1990). A mineral distribution based on mole-, weight-, and volume-percentage was calculated as a synthetical composition (Wolf and Hettema, 1995).

Furthermore, new polished thin sections were used to verify the XRD/XRF-results by petrography. Considering that grain and pore size are significant variables contributing to permeability, the grain and pore size distribution and mineral distribution were analyzed for improving the previously mentioned experiments. The 2D grain size distribution was reconstructed into a 3D sorting. Additionally, a series of micro-CT scans and regular CT scans were performed to reconstruct a more realistic 3D grain diameter and pore throat/bodies distribution, where the results on mineral spread, porosity and permeability were compared with the previous results. The micro-CT scanner has a resolution of five micrometers and is therefore able to recognize clay minerals.

The rock's physical and chemical properties are in addition affected by the surface charge. This is a property of Bentheimer sandstone in contact with electrolyte solution, since it controls adsorption/adhesion from the electrolyte (Calvo et al., 1996). The surface reactions and the concentration of the "potential determining ions" are essential to determine the interfacial behavior. In addition, the effects of clay minerals and iron-oxides/-hydroxides may cause "contradictory" results, but can be quantified. The specific surface area, a parameter necessary for the correct interpretation of the electrical behavior of Bentheimer sandstone, was measured using the nitrogen adsorption method.

In essence, the main contribution of this paper is to combine all the petrophysical properties determined with the mineral composition. The 3D reconstruction of the rock's grain and pore structure gives an irregular network that represents the flow path and can be used to predict permeability and resistivity (conductivity of rock) without conducting any direct laboratory measurements of either parameter.

## 2. Literature overview

Over the past 50 years, the Bentheimer sandstone has been characterized by various German authors (Füchtbauer, 1963; Füchtbauer, 1955; Kemper, 1968, 1976; Stadtler, 1998). They have investigated, interpreted and summarized basic geology, structural setting, lithology and depositional environments of the Bentheimer sandstone. Correlations of sedimentary facies, diagenetic features and reservoir modeling was done by Swedish scientists (Malmborg, 2002; Mansurbeg, 2001). Moreover Wonham et al. (1997) made an assessment of the reservoir characteristics of the Bentheim sandstone at outcrop in the Bad Bentheim area and in the subsurface in the Röhlermoor field; Mutterlose and Bornemann (2000) described distribution and regional settings of the formation and recently Dubelaar and Nijland (2015) characterized geology and petrophysics of it as a building stone. However, in prior works, the main focus was either on geological and paleontological settings or on a certain parameter like, porosity and permeability (Al Ghamdi and Arns, 2012; Doughty and Tomutsa, 1996; Johns et al., 2003; Mansfield and Issa, 1994; Mitchell et al., 2008; Swaid et al., 1997), mineral composition (Al-Muntasher et al., 2010; Kemper, 1968, 1976; Maloney et al., 1990; Mayr and Burkhardt, 2006; Van Baaren et al., 1990), as well as pore throat/bodies size distribution, that is described in much extended way and in detail.

Over the past decades, many permeability measurements have been performed with the same Ruska permeameter (Maloney et al., 1990; Van Baaren et al., 1990; Wolf and Hettema, 1995). Bentheimer sandstone, as a whole, has been considered in experimental and modeling work focusing on its bulk behavior, where only the grain and pore aggregates and not the grains and pores themselves were

taken into account (Blöcher et al., 2014; De Boever et al., 2013; Ersland et al., 2010; Fernø et al., 2013; Klein et al., 2001; Kvamme et al., 2007; Smeets and Golombok, 2010). Now CT scanning, MRI and confocal microscopy are increasingly applied when studying the rock/fluid/gas–oil behavior of permeability, capillarity and wettability in greater detail. The matrix distribution of the individual grains and minerals is considered to be of greater importance. Especially now, image analysis methods are able to distinguish spatial matrix and pore properties at micrometer scale (Bakke and Øren, 2013; Bultreys et al., 2013; Louis et al., 2005; Nguyen et al., 2009; Ramstad et al., 2010; Thovert and Adler, 2011). Grain/pore size and pore throat distribution, pore coordination numbers and specific pore space and surfaces can be more accurately calculated at micro- and nano-level. Moreover, minerals can be assigned to volumes and coordinates in a sample so that petrophysical parameters such as dielectric constants can be calculated.

A lot of other data such as grain size distribution, mineralogical content, mechanical behavior can be found in the literature, but mainly as additional information provided by author as a background to conducted research. Researchers were determining particular properties of Bentheimer sandstone, while conducting investigation on oil recovery (Al-Futaisi and Patzek, 2004; Amro and Kessel, 1996; Berg, 2012; Borschinsky and Kulke, 1992; Doughty and Tomutsa, 1996; Feali et al., 2012; Fernø et al., 2013; Fodisch et al., 2013; Frette and Helland, 2010; Hansen et al., 1999; Hesselsink and Faber, 1981; Holt et al., 1995; Maldal et al., 1997; Maldal and Hoiland, 1997; Mansfield et al., 1992; McLendon et al., 2014, 2012; Mitchell et al., 2008; Nguyen et al., 2009; Olafuyi et al., 2011; Reichenbach-Klinke et al., 2013; Romanenko and Balcom, 2013; Sheppard et al., 2003; Shoaikaveh et al., 2014; Sigel et al., 2012; Simjoo et al., 2013; Skauge et al., 2012; Smeets and Golombok, 2010; Taubøel et al., 1995; Wever et al., 2013; Xiao and Balcom, 2014; Zhou et al., 2012a, 2012b), formation of gas hydrates (Ersland et al., 2010; Kvamme et al., 2007, 2009, 2006), distributions of fluid velocities (Mansfield and Issa, 1996).

## 3. Geological setting

The proper understanding of the physical properties of Bentheimer sandstone requires an understanding of the depositional and diagenetic history. The physical properties are a function of provenance, transport depositional environment, and any diagenesis that took place.

Bentheimer sandstone occurs in the south western part of the Lower Saxony Basin (Fig. 1) and it outcrops along the east of the Dutch–German border, mainly within the area outlined by Meppen, Adorf, Nordhorn, Bentheim and Ochtrup (Betz et al., 1987; Füchtbauer, 1955; Kemper, 1968, 1976; Kemper and van der Burgh, 1992; Malmborg, 2002; Mansurbeg, 2001; Mutterlose and Bornemann, 2000; Stadtler, 1998; Wonham et al., 1997). It belongs to the late Early Valanginian of the Lower Cretaceous (Kemper, 1976) and was deposited in one of the Lower Cretaceous basins to the north of the London-Brabant Massif and the Rhenish Massif. According to Dubelaar and Nijland (2015), for the duration of Valanginian times, a slow eustatic sea-level rise caused flooding of the Lower Saxony Basin. As a result marine conditions were established, which is proven by the presence of ammonites *Platy-lenticeras* (Mutterlose and Bornemann, 2000). As reported by Hinze (1988) the Valanginian age deposits are distributed preferentially along salt anticlines. The overall consensus is that the initial Valanginian transgressions (in the early and the earliest late Valanginian) progressed from the southern North Sea through the East Netherlands High to the eastern parts of the Altmark-Fläming Basin. As a result the main area of marine offshore sedimentation took place in the Emsland Basin. Based on palaeoecological and

palaeobathymetric studies, during regressive-transgressive Valanginian cycles the progression of two sandstones (the Bentheim and the *Dichotomites*) occurred into the basin as the intercalated fragments of a thick deposition of marine clay stones.

These sandstones are hundreds of kilometers long and few kilometers wide barrier sand and form a rim around the Lower Saxony Basin (Fig. 1). The hinterland sources are mainly of Bunter sandstone from the Munsterland Block, the Rhenish Massif and the Friesland High (Kemper and van der Burgh, 1992). In accordance with micropalaeontological data, the Bentheim Sandstone was deposited from the upper part of the Lower Valanginian to the lowermost Upper Valanginian. The formation is a sequence of massive shallow marine sandstones deposited in a deltaic to inner/middle-neritic setting. The abundant coarse clasts and lignite fragments are indications of a high-energy, near-shore depositional environment (Mutterlose and Bornemann, 2000). The Bentheim sandstone overlies the Bentheim Claystone Member. Locally, in the absence of the Bentheim Claystone Member, the lower boundary of the formation has unconformable conditions due to contact with the Coevorden Claystone Formation (Niedersachsen Group). At the top, Bentheimer sandstone is conformably overlain by the Ruinen Member of Vlieland Claystone Formations, which consists of a thin sequence of fossiliferous claystones topped by thin silt or sandstones. In the absence of the Ruinen Member due to palaeogeographically elevated settings, it is covered by the Westerbork Member, which belongs to Vlieland Claystone Formations and is represented by glauconitic claystones to marls with marine fauna. The transition of Bentheimer sandstone towards the east into the Vlieland Claystone Formations (marine shales) created stratigraphic oil traps (the Bramberge Field) (Fig. 1).

Since the 11th and 12th centuries, Bentheimer sandstone has been mined in Bentheim county in 22 quarries. According to

Wonham et al. (1997) all outcrops located in the Emsland area are associated to east-west striking salt anticlines. Today, it is excavated mainly at two locations: (1) in the Romberg Quarry in Gildehaus, where the beige-colored sandstone with the brand name "Gildehaus" can be found; (2) next to Bentheim, south of the Romberg Quarry, where outcrops are rich in the characteristic reddish sandstone that exists under the name "Bentheim".

In our work and previous studies (Al-Muntasher et al., 2010; Blöcher et al., 2014; Bultreys et al., 2013; Dresen et al., 2010; Fernø et al., 2013; Kemper, 1968, 1976; Klein et al., 2001; Klov, 2000; Malmborg, 2002; Maloney et al., 1990; Mansurbeg, 2001; Milsch and Blöcher, 2013; Stanchits et al., 2009; Van Baaren et al., 1990), type locality has been sampled in the Romberg Quarry. Essentially, more descriptive information about the lithological units in which the samples originated is included.

A first attempt at a unit – lithographic interpretation of the Bentheimer Formation was published by Kemper (1968) and Wonham et al. (1997) completed the division of this formation, and gave a detail interpretation of the Unit I. Bentheimer sandstone has been divided there into three different lithographic units (I–III) that can be distinguished by rock mass classification and, in our case, by variation in color (in the web version) and also the strength of the grain framework ( friability) (Figs. 1 and 2). Unit I – Lower Bentheim Sandstone, deposited under high energy conditions and consist of large cross-bedded units. It was subdivided by Wonham et al. (1997) into four subzones: (1) at the bottom, the Lower bioturbated zone with thick sands at the bottom; (2) the Basisbank with a bioturbated zone (12 m); (3) a Heterolithic facies with several thin layers (~1 m) intercalated by thin shale layers in the middle, and (4) at the top, the "Haupt sandstein" or main sandstone (~20 m), a barrier sand with low angle stratifications, deposited by currents parallel to the coast. Unit II represents Romberg Shale, a

Emsland area				
System		Lithostratigraphy	Type locality (Romberg)	Sequence stratigraphy
Lower Cretaceous	Valanginian	Upper	Grenz Sandstone	
			Unnamed unit	
			Dichotomites Sandstone	
			Erectum Clay	
		Lower	Upper Bentheim Sandstone	Bentheim Sandstone 3
			Romberg Clay	
			Haupt Sandstone	
			Heterolithic Facies	
			Basisbank	
			Lower bioturbated zone	
		Platylenticeras Clay		

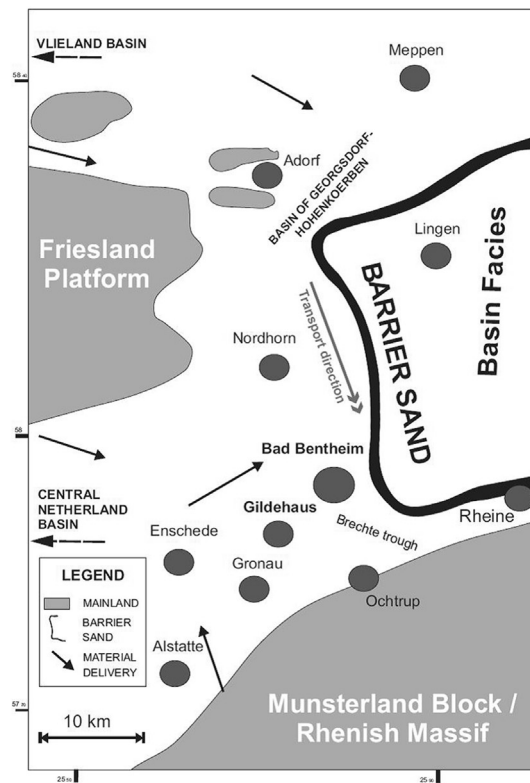


**Fig. 1.** (table) The lithostratigraphic and sequence stratigraphic division of the Valanginian in Emsland area (Mutterlose and Bornemann, 2000); (map) Sedimentary interpretation of the Lower Cretaceous and Bentheimer sandstone environment, revised after Kemper and van der Burgh (1992), Mutterlose and Bornemann (2000) and De Jager and Geluk (2007).

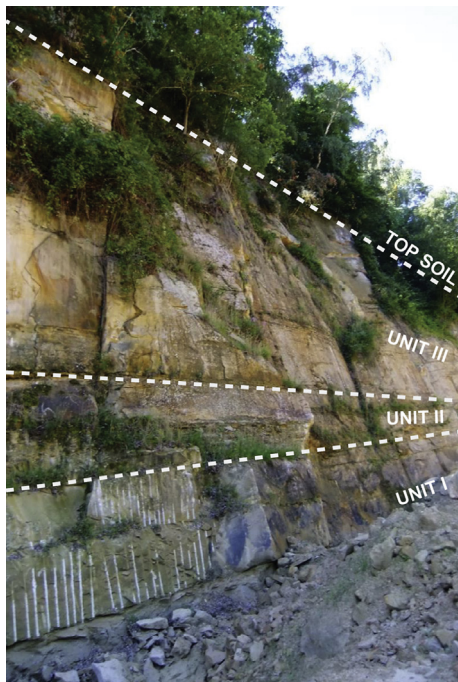


**Fig. 2.** The lithographic units in the Gildehaus–Romberg quarry. It represents three visibly different units of the Bentheim formation. Unit I represents the Lower Bentheim sandstone; Unit II represents the intermediate Romberg – fine sandy shaly layer (~4 m). Unit III is Upper Bentheim sandstone.

fine sandy shaly layer (~4 m) (Kemper, 1976), showing the results of intense bioturbation (i.e., Arenicolites, Skolithos, Ophiomorpha) (Jeremiah et al., 2010). Unit II is overlain by the Upper Bentheim sandstone that was deposited under lower energy conditions.

The samples normally used in laboratory work originate from the Unit III. Note that the framework mineralogy of Bentheimer sandstone at the field scale can to some extent vary with increasing burial depth, temperature and circulation of acidic fluids, originating from the maturation of hydrocarbons. Moreover, in the near geological history, groundwater and glacial effects may have changed the sandstones, resulting in leaching of K-feldspars and limestone and further creation of secondary porosity. Therefore, the samples from the Romberg Quarry less representative of the same reservoir under in-situ conditions.

#### 4. Materials

In the past 50 years, around the world and in our laboratory, Bentheimer sandstone characteristics such as porosity, permeability, grain size distribution, pores bodies and throat distribution etc. have been obtained from laboratory measurements on plugs, from statistical reconstruction of 2D thin section images and high resolution X-ray microtomography (micro-CT scans) (Bakke and Øren, 2013; Bultreys et al., 2013; Dautriat et al., 2009; Ersland et al., 2010; Halisch, 2013b; Hassan, 2012; Kemper, 1968, 1976; Klov, 2000; Louis et al., 2005, 2003; Maloney et al., 1990; Ramstad et al., 2010; Reinicke, 2009; Thovert and Adler, 2011). The mentioned methods partly cover each of the spatial and petrophysical parameters, i.e., pore and grain size distribution and porosity.

##### 4.1. Sample materials

For this study four series of samples with different dates of origin have been used:

- Old core samples (OS) – collected at the Romberg Quarry in 2007;
- Intermediate core samples (IS) – collected at the Romberg Quarry in 2012;
- Fresh core samples (FS) – collected at the Romberg Quarry in 2013;
- Four fresh samples were collected at 4 different locations of the Romberg Quarry: FSQI–IV (Fig. 3a).

The samples of Bentheimer sandstone (type Gildehaus) were collected from the Romberg Quarry in Gildehaus (the Bentheim 3 member). They were gathered at various times and used during experimental work over the past ten years. The sets of laboratory cores and blocks were arbitrarily drilled in the quarry samples, but according to the specifications required for the various measurement programs (Figs. 2 and 3). The variation in data collection over the years, and the use of different wet/dry porosity/permeability measurements, made use of the statistical “iterative sampling” approach for an unbiased conclusion.

#### 4.2. Sample textures, structures and mineralogy

**Thin sections (Fig. 3b):** For texture characterization of the grain framework and pores, samples were impregnated with a blue dye or fluorescent resin. Thereafter, they were used for the preparation of glass covered and polished thin sections. The advantage of polished, uncovered thin sections is the highly reflective surface and absence of the interfering effects of glass plates, i.e., a sharper boundary between pores and grains can be distinguished. The thin sections are used to qualify and quantify the mineral content (grain framework), grain/pore size distribution, and grain contacts by using a polarized light microscope and fluorescing option combined with an incident light microscope.

### 5. Methods

#### 5.1. Image analysis procedures

##### 5.1.1. 2D and 3D discrete CT-image analysis methods

Image analysis of polished thin sections and stacked CT-images have been used to determine the size distribution and other spatial parameters of the grains (e.g. volume, area, perimeter, length, width and orientation).

##### 5.1.2. 2D-microscopy

2D thin sections image analysis: By using a polarization microscope with parallel and crossed nicols, thin sections were transformed into binary images and analyzed on their spatial characteristics by using a Leica Qwin™. The 2D grain size distribution results were recalculated to an empirical 3D sphere size distribution by stereological methods with a numerical method for fixed thickness steps (Gubbins, 2009), thickness intersection planes based on Wicksell transform (1925), and the Russ conversion method (1991). Twenty cuttings with a random orientation show a data variation providing values for the isotropy and heterogeneity of the grain size, orientation and texture. The image processing steps and generation of the size distribution are shown in Fig. 4a.

##### 5.1.3. 3D discrete image analysis methods

A Phoenix Nanotom™ Micro-CT scanner ( $\mu$ CT) of 180 kV/15 W, with a nanofocus computed tomography system, was used to create 2D stacks of Bentheimer sandstone. It is equipped with a 5 mega-pixel detector and a maximum voxel resolution of  $<0.5 \mu\text{m}$ , which was used for our samples. The pencil type sample, 120 mm in length and with a diameter of 10 mm (or ca. 50 grains width),

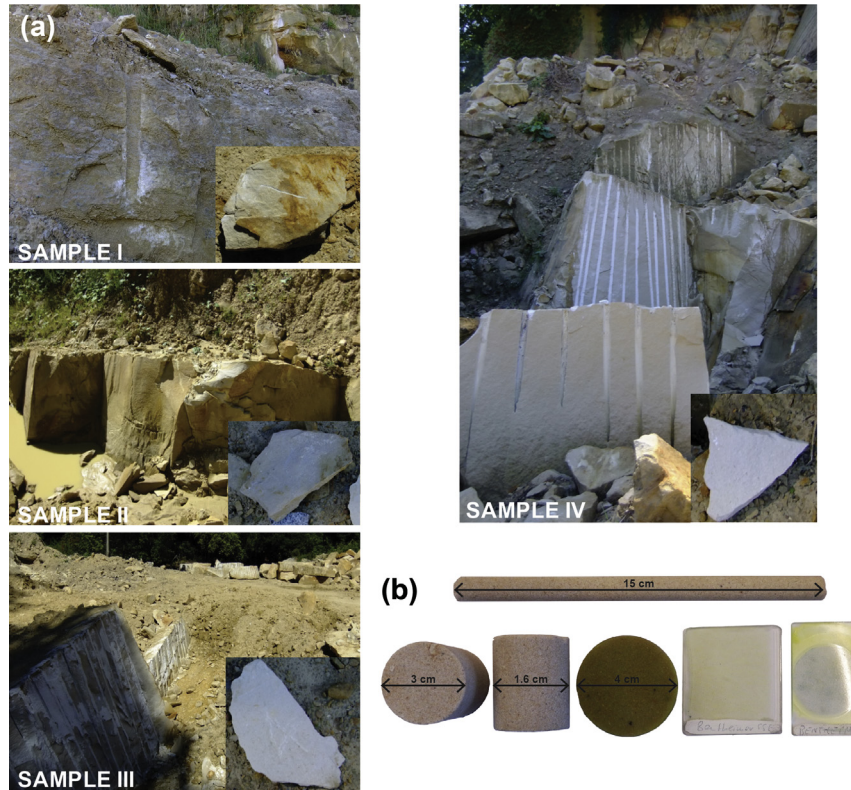


**Fig. 3.** (a) Sample locations in the Gildehaus–Romberg quarry FQI–IV. (b) Representation of the rock sampling of Bentheimer cores and thin sections. The yellow colors are the fluorescing dye in the pores. (For interpretation of the references to colour in this figure legend, the reader is referred to the web version of this article.)

provides a representative number of grains and associated pore framework. The stacked 3D volumes were reconstructed with AVIZO™ software. The image processing steps and generation of the size distribution are based on dilation/erosion algorithms for body separations (see flow chart, Fig. 4b). Pore bodies and throats volumes were identified and connected to the original image voxels. A spherical shape of the pore bodies is assumed based on area and perimeter, and overlapping is taken into account. Subsequently, the effective pore body diameter is computed. An effective throat radius is calculated respectively, with a modification that the throat volume is assigned to a corresponding cylindrical volume. The height of the cylindrical structure is equivalent to the maximum distance computed between any two spheres representing a pore body.

The spatial categorizations (pore/grain-matrix) are used to define in 3D and 2D the specific grain surfaces, pore volumes, etc. as needed for the permeability model. In 3D, permeability computations are based on the modified Kozeny–Carman equation (Eq. (1)). According to Ruzyla (1986), a 3D pore network with complex cross-sections in shape can be simplified into a 2D geometrical model of average constant areas presuming that the heterogeneity of the matrix in all directions is the same. It relates permeability ( $K$ ) to porosity ( $\varphi$ ), specific surface area ( $S_{sa}$ ) and tortuosity ( $L_e/L$ ) of the pore system by the following equation:

$$K = \frac{\varphi^3}{K_o \left( \frac{L_e}{L} \right)^2 (1 - \varphi)^2 S_{sa}^2} \quad (1)$$

where  $K_o$  is the Kozeny constant, an empirical constant that depends on the cross-sectional shape of the flow paths. For the thin section calculations, Ruzyla's conversion is used:

$$K = \frac{\varphi^3}{c(1 - \varphi)^2 \left( \frac{4P_p}{\pi A_p} \right)^2}, \quad (2)$$

where  $P_p$  is the pore perimeter,  $A_p$  is the pore area and  $c$  is a constant associated with the tortuosity ( $L_e/L$ ).

The spatial results on grain bodies, e.g. area, perimeter, contact number and contact area as a part of the total grain surface, are used for grain density specification. The spatial results on pore volume and pore body measurements are translated to pore area distributions, perimeter, coordination numbers, pore throat diameter, etc. These distributions can be used for the construction of pore/grain frameworks in Monte Carlo simulations on permeability and capillarity. This subject will not be discussed further in this article.

In addition, the orientations of the long axes of grains were measured on thin sections and SEM images, and further plotted in the circular histogram to identify preferred directions.

## 5.2. Laboratory procedures

### 5.2.1. XRD/XRF mineral composition

Samples for X-ray diffraction and X-ray fluorescence were pulverized to a 2 μm powder and used for the determination of mineral composition and element oxide distribution. The XRD was recorded in a Bragg-Brentano geometer with a Bruker D5005™ diffractometer, equipped with a Huber incident-beam monochromator and a Braun PSD detector. To prove the identification of authigenic minerals, some samples were examined using an electron microprobe JEOL 8800 M JXA Superprobe (1993). The XRF measurements were done with a Panalytical Axios Max WD-XRF

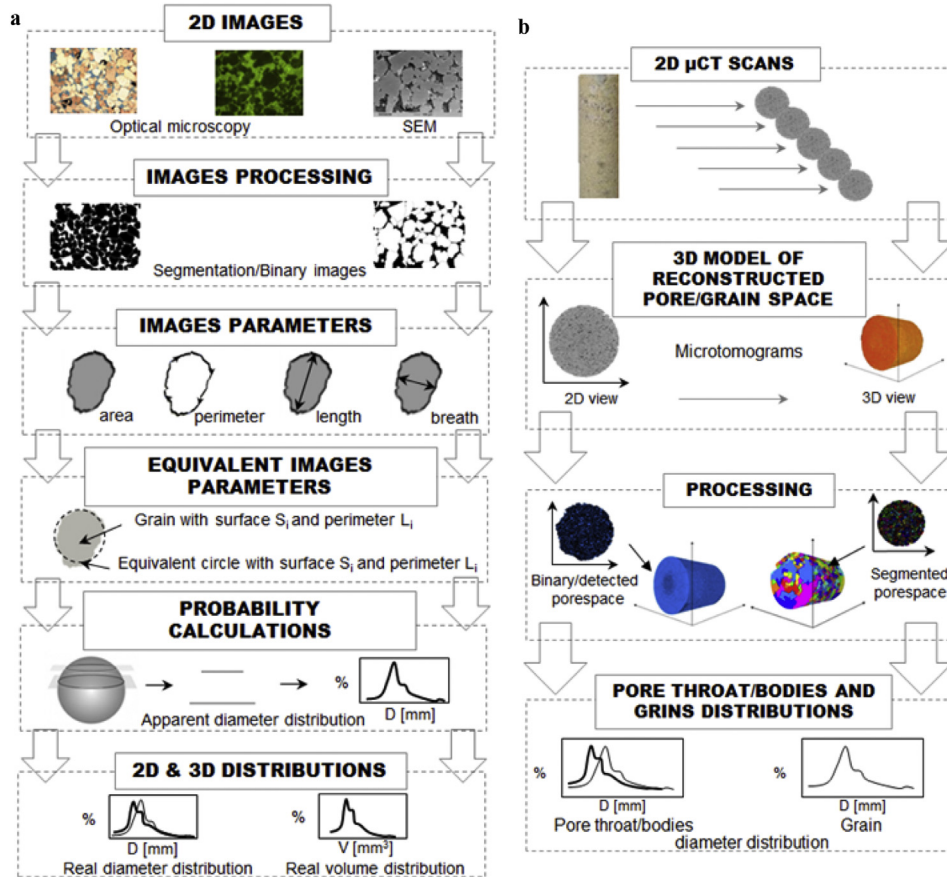


Fig. 4. (a – left) Flow chart spatial results on 2D thin sections image analysis; (b – right) 3D micro-CT scan discrete image analysis.

spectrometer, measuring the element oxides and elements with an estimated accuracy of 2% that are presented with >0.5 wt%.

#### 5.2.2. Porosity and absolute permeability

Porosity and permeability for Bentheimer sandstone were determined on cylindrical samples 30 mm in diameter and 36 mm in length (Fig. 3b).

- Dry porosity tests were conducted with a gas expansion Ultra Pycnometer 1000 (Quantachrome Instruments™) using Boyle's gas expansion law. The resulting matrix volume values ( $1-\phi$ ) provide the bulk density ( $\rho$ ) and effective porosity ( $\phi$ ).
- The permeability of dry cores was measured with N<sub>2</sub> using a Ruska gas permeameter; next, the samples were saturated with de-ionized water in a desiccator and weighed before and after saturation to calculate the wet porosity, following Archimedes' law. The cores were kept submerged to avoid air intrusion during measurements. Thereafter, absolute wet permeability was calculated from liquid permeameter experiments by using the flow velocities and differential pressure, following Darcie's law (Ruska Instruments™).

#### 5.2.3. Mechanical properties

The uniaxial mechanical properties of wet and dry Bentheimer sandstone samples (stress-strain behavior) were examined using the ASTM D2938-95 and D 3148-96 Standard Test Procedure (STP) for the determination of unconfined compressive strength, Young's modulus and Poisson's ratio. The samples were loaded until failure while the axial load and vertical and horizontal deformation were

monitored. The load was applied with a constant stress rate in between 0.5 and 1 MPa/sec (1% accuracy).

For four fresh cylindrical samples (FS1–4), with shape tolerances according to ASTM 4543, but with different height to diameter ratios ( $L/D$ -ratios in between 2 and 1), the tangent modulus  $E_t$  was measured at a stress level of 50% of the assumed yield stress, and the strain modulus  $E_{ave}$  was determined from the average slope of the straight line part of the stress–strain curve.

#### 5.2.4. Dielectrical behavior

To determine the surface behavior, potentiometric titration experiments were conducted. The procedure is as follows: (1) Before starting the dielectrical measurements, a given amount of solid dissolved in electrolyte was stirred with a teflon magnetic stirrer for 24 h, followed by potentiometric titration to measure the acid/base properties of mixtures. The pH values of different rock volumes (0.5 g, 5.0 g, and 10 g) showed an increase in the pH of the mixture. Then potentiometric titrations were performed in a nitrogen atmosphere (continuously stirred), adding HCl or NaOH to the solution cell in 10–15 steps of 2.0 ml each. The pH data were recorded at 5 min time lapses (5 min) with the stirrer switched off. Titrations were performed for 3 different masses of solids (0.5 g, 5.0 g and 10 g) in 75 and 100 ml of H<sub>2</sub>O (demineralized and degassed), and in 75 and 100 ml of 2.2 mol/dm<sup>3</sup> NaCl solution; (2) Additionally, titrations of blank electrolytes were performed for calculation purposes. The initial pH was established by addition of 8 ml 0.1 mol/dm<sup>3</sup> NaOH; 0.1 mol/dm<sup>3</sup> HCl was used as a titrant.

The pH-dependent surface charge ( $\sigma_0$ ) was calculated with following Equation (3):

$$\sigma_0(pH) = -\frac{F \cdot (\Delta n_{sol,H^+}(pH) - \Delta n_o)}{Ma_s} = \frac{f_{surf}(pH)}{Ss}, \quad (3)$$

where  $F$  is the Faraday constant ( $F = 96500$  C/mol),  $M$  is sample mass;  $Ss$  surface area and  $\Delta n_o$  the pH-dependent amount of acid/base consumed. The dissolution effect ( $\Delta n_{sol,H^+}$ ) was obtained by comparison of the balance of protons and hydroxyl ions in the potentiometric titration of Bentheimer samples with blank potentiometric titration results:

$$\Delta n_{sol,H^+}(pH) = \Delta n_{acid\backslash base(BS)}(pH) - \Delta n_{acid\backslash base(blank)}(pH) \quad (4)$$

where  $\Delta n_{sol,H^+}$  (pH) represents the balance of protons and hydroxyl ions in titration of solid with electrolyte titration.

### 5.2.5. Specific surface area

The specific surface area, a parameter necessary for determination of the homogeneity of the sample and the correct interpretation of the electrical behavior of Bentheimer sandstone, was measured. The specific surface areas of rock samples were obtained in two ways: (1) at pore level, discussed previously, from thin section analysis on a consolidated Bentheimer sandstone sample, and (2) at electron level, by adsorption of nitrogen, at low temperatures (77 K).

Before each measurement, the Bentheimer samples were degassed at 150 °C for at least 24 h. The nitrogen adsorption of samples was measured with a Micrometrics Gemini™ system. The adsorption behavior in porous material is related to both fluid wall interactions and the attractive interactions occurring among the fluid molecules. It results in multilayer adsorption and the existence of capillary condensation in the pore space. The capillary condensation, a process that occurs mainly in small capillaries and pores at vapor pressures below the saturated vapor pressure  $p_o$ , can be predicted by the Kelvin Equation (5):

$$RT \ln \frac{p}{p_o} = \gamma V_m \left( \frac{1}{r_1} + \frac{1}{r_2} \right) \quad (5)$$

where  $p_v$  stands for the vapor pressure above the curved surface,  $p_o$  is the pressure above the flat surface,  $V_m$  represents the molar volume of the liquid,  $r_1$  and  $r_2$  the low principal radii of curvature, and  $\gamma$  the surface tension of the liquid surface (Gubbins, 2009). For the purpose of the experiment, we kept the temperature constant and, by varying the external gas pressure and simultaneously monitoring and quantifying adsorption at certain pressures, we obtained the adsorption isotherm.

The specific surface data was calculated using the BET sorption theory (Brunauer et al., 1938). The obtained specific surface area represents the “external” surface area, since the penetration of the interlayer of smaller clay particles surfaces by weakly adsorbed nitrogen is not entirely possible.

In addition, to support this investigation, a data set was obtained from literature dealing with the petrophysical and petrographical properties of Bentheimer sandstone. We collected data on the mineralogical composition of sandstone samples obtained from Romberg Quarry. We standardized and compared in graphical form the available data on pore and grain size distribution obtained by different methods, starting from microscopic and macroscopic image inspection, image analysis and mercury intrusion. Furthermore, we gathered information obtained by other researchers about porosity and permeability values.

## 6. Results and discussion

### 6.1. Petrography and mineralogy

#### 6.1.1. Texture and structure

Polarization microscopy, SEM and XRD show that Bentheimer sandstone consists predominantly of monocrystalline quartz with authigenic overgrowth, detrital polycrystalline feldspars, authigenic clay as a weathering product of original feldspars and dispersed organic matter with some iron-(hydr)oxides (Table 1). Weathering and dissolution of feldspars occasionally created some intragranular porosity – depositional pores and oversized pores, i.e., a moldic type of porosity. The secondary minerals (mainly kaolinite and smectite) clogged pores and necks (pore lining and filling type); however, quartz overgrowths are the main reducers of the primary intergranular porosity. The iron (hydr)oxides concretions are secondary products filling former fossils and pyrite spaces.

**6.1.1.1. Orientation.** The SEM and thin section images and statistical analysis indicate random orientation of the elongated grains (Fig. 5). As the permeability is normally higher in the direction of the orientation of the grains, here random orientation of the grains indicates the lack of a preferred direction of permeability. Thus, homogeneous grain aggregates may be expected.

#### 6.1.2. Minerals

The minerals are described in order of abundance:

**6.1.2.1. Quartz** (91.70 wt%). The grain shape is usually rounded to subrounded. In the grains framework, quartz cement is the main reducer of pore space due to diagenetical syntaxial overgrowths around the original detrital quartz grains (Fig. 6a and b). The boundaries between the overgrown grains are well marked, because of clean rims of epitaxial cement with clay- and fluid-inclusions (Fig. 6a and b). In addition, traces of cementation by pressure solution have been observed (Figs. 6a and 8b). Furthermore, grains boundaries migrations are visible in the form of coarsening of quartz grains sizes into chert and largely unstrained quartz composed on small recrystallized grains (Fig. 6c).

**6.1.2.2. Feldspars** (4.86 wt%). The brownish K-feldspars exhibit a distinct cleavage (Figs. 8c and 9a–c), which is even more distinguished by weathering to small patches of carbonates and clays (among others, kaolinite and illite-sericite). Weathering occurs mainly along the cleavage planes (Figs. 6c and 9) and at the grain rims. The elongated and angular shape of the feldspars grains is a result of the damage along cleavage planes during sedimentary transport.

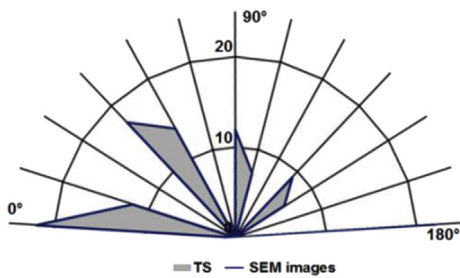
**6.1.2.3. Clay minerals** (2.68 wt%). These mainly consist of kaolinite, montmorillonite and illite-sericite. Kaolinite and illite-sericite are weathering products. Some inclusions in the rims of quartz overgrowths prove that primary clay is present. The SEM images show predominantly book-type pore lining and pore filling kaolinite. Illitic fractions occur as a pore lining and as a grain replacement (Fig. 10 a,b).

**6.1.2.4. Pyrite and iron (hydr)oxides** (0.17 wt%). Occasionally these can be recognized as frambooidal shapes between the grains as a secondary phase (Fig. 10c). As pyrite is unstable in oxidizing environments, in the outcrop samples, they are often changed to an amorphous hematite or goethite mineral type. Hematite pore filling was identified in small spots, which can be recognized in the thin

**Table 1**

XRD-mineralogy of Bentheimer sandstone of the Romberg Quarry in Gildehaus.

Mineral		Al-Muntasher et al., 2010	This study (al-Muntasher et al.)	Maloney et al., 1990	Van Baaren et al., 1990	Mayr and Burkhardt, 2006	Kemper 1976 after Holl (Mayr and Burkhardt, 2006)	
		wt %	wt %	Vol %	wt %	wt %	wt %	Vol%
Silicate minerals	Clay	Quartz	88	91.70	91.62	97.50	95	90–96 (+2 chert)
		Illite	2				3	>90 Acc.
		Kaolinite	2	2.50	2.55	0.50		
		Montmorillonite		0.18	0.18			
		Chlorite	1					
	Feldspar	Plagioclaste	Albite (na)	2		2	2	2–4
			K-feldspar		4.86	5.03		Acc.
			Microcline	3				
			Siderite			T		
			Dolomite	2	0.26	0.24 T		
Carbonate mineral			Calcite		0.15	0.14 T		
			Hematite/Gibbsite		0.16	0.08		Acc.
Oxide mineral	Fe sulfide mineral	Rutile			0.03	0.04		
		Pyrite			0.01	0.01		Acc.
Fe sulfide mineral		Ca-phosphate			0.07	0.06		
		Halite (nacl)			0.03	0.04		
		Sum	100.00	100	100	100	100	100

**Fig. 5.** Grain orientation distribution of length.

sections as random brownish spots in the sandstone cores (Fig. 7a). Besides, occasionally larger (mm to cm scale) iron (hydr)oxide inclusions are present, hidden as lumps in whole cores. Pyrite occurring as the characteristic early diagenetic mineral confirms the marine sedimentary environment.

Based on the sections and SEM it can be concluded that authigenic quartz overgrowths reduce the average pore throat size. Moreover, the alteration of unstable minerals, such as feldspars may lead to creation of the permeability reducing secondary porosity. However, the small amounts of K-feldspar (4.86 wt%) did

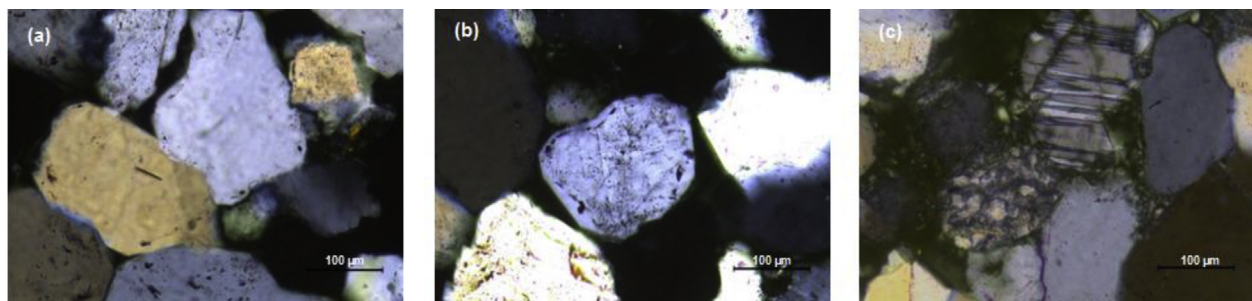
not generate enough of clays precipitation to significantly affect the bulk reservoir porosity and permeability, except a migration of clays results in clogging zone production, which incidentally happens.

The XRD and XRF analysis showed some minor differences in the results. In most studies (Kemper, 1968; Maloney et al., 1990; Mayr and Burkhardt, 2006) the wt% of quartz content is in the range of 90–98%, and only Al-Muntasher et al. (2010) reported 88 wt% of quartz in Bentheimer samples. In most of the samples, feldspar component was recognized (2–5 wt%), with the difference that in this work and other studies (Kemper, 1968; Maloney et al., 1990) orthoclase was found, whereas Al-Muntasher et al. (2010) showed the existence of albite and microcline. This is a result of the XRD interpretation. We suggest summing the feldspar minerals to a total of 4.86 wt%. For all the studies presented in the table, kaolinite was reported as a main clay representative (0.5–2.5 wt%), apart from Van Baaren et al. (1990), who found only illite.

## 6.2. Petrophysical data

### 6.2.1. Pore and grain size distribution

CT scans and thin sections were used to reconstruct 3D grain size and pore size distributions. The methods used have been discussed previously.

**Fig. 6.** Thin-section optical micrographs that represent: (a) overgrowth cement on rounded detrital quartz grains and pressure solution contacts; (b) detrital quartz grains with overgrowths in crystallographic continuity and different generation of fluid inclusions: at the boundary between the detrital quartz grain and the overgrowths and along the quartz micro fractures; (c) unstrained quartz, alkali feldspar, and illitic fractions incorporated by bioturbation and mechanical infiltration.

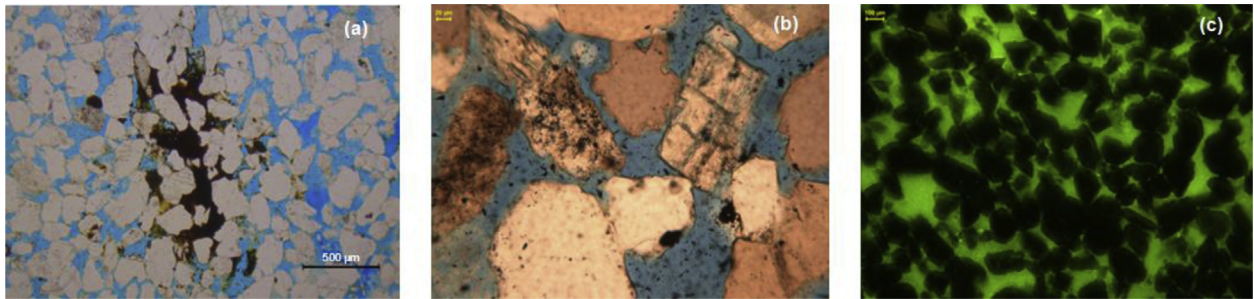


**Fig. 7.** Thin-section optical micrographs that represent: (a) loosely packed quartz and weathered feldspar and pore filling with hematite; (b) weathering of a feldspar; (c) fluorescing view providing a binary view of the pore framework (green) and grain framework (dark). (For interpretation of the references to colour in this figure legend, the reader is referred to the web version of this article.)

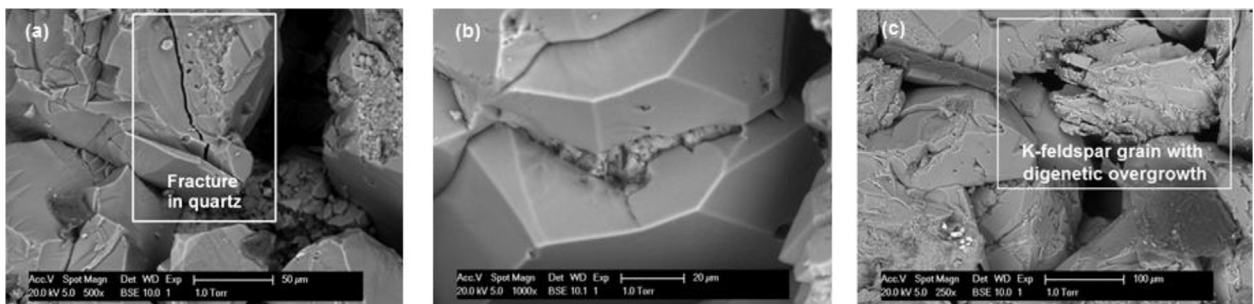


**Fig. 8.** SEM microphotographs that represent: (a) fracture in quartz grain; (b) quartz overgrowth; (c) K – feldspar grain with digenetic overgrowth.

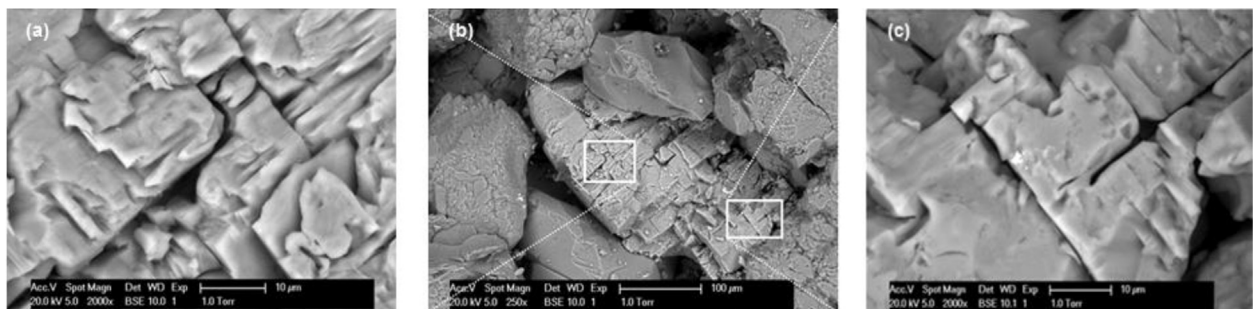


**Fig. 9.** SEM microphotographs of the K – feldspar grain.

#### 6.2.2. Pore bodies and pore throat distribution by CT scanning

The pencil size Bentheimer samples (Fig. 3b) were scanned to get high resolution images (5 μm) for stacking. The pore space was obtained in two ways: first as a gray level threshold binary grain and pore network followed by a series of separation algorithms to reconstruct the discrete pore/grain bodies and associated spherical pore throats. The results of the binary file were stacked to three-

dimensional data sets to measure size distributions. Fig. 11a–d show an example of the randomly selected first reconstruction slices of the analyzed scans that represent grains and pore space, pore throats and pore bodies respectively. The final result of reconstruction – the 3D view of the rendered pore space and grain framework – is shown in Fig. 12. Additional statistical measurements provided us with pore bodies and throat diameter

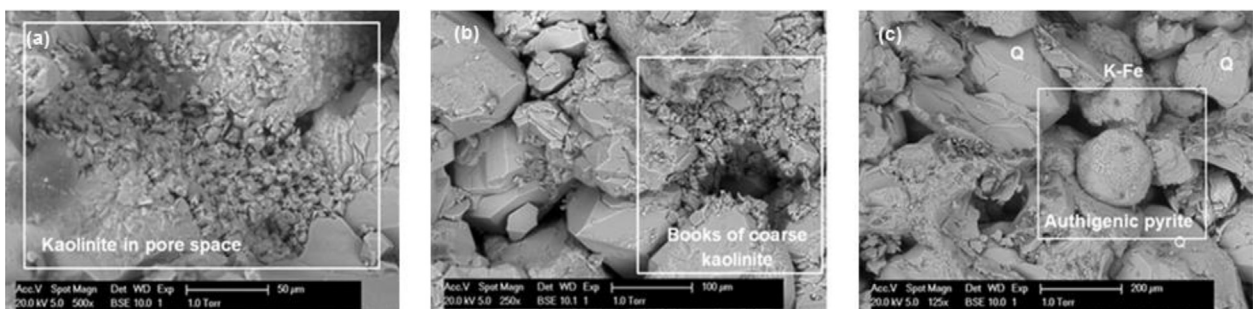


**Fig. 10.** SEM microphotographs that represent: (a) kaolinite; (b) books of coarse kaolinite partly occluding pores; (c) pyrite frambooids.

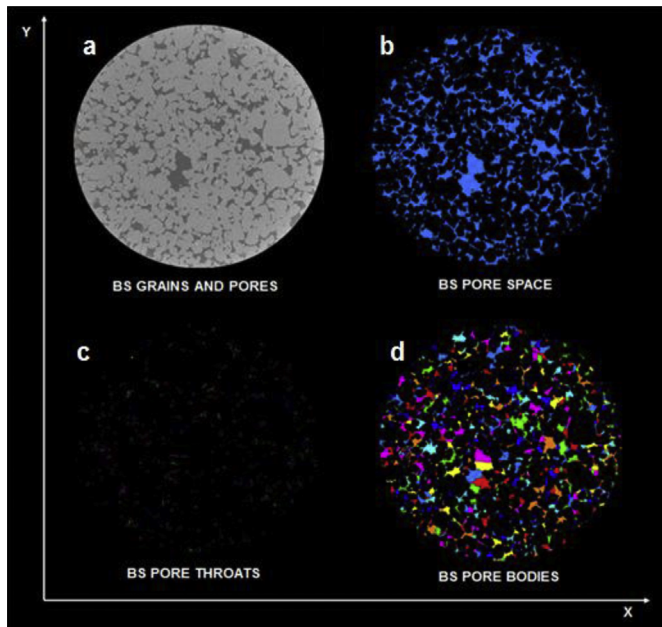


**Fig. 11.** Micro-CT images of porous media. They represent cross-sectional images of (a) Bentheimer sandstone grains. Pores are in dark gray, and light gray represents mostly quartz grains. The small white spots represent feldspars; (b) Bentheimer sandstone pore space that poses 0.24 of volume; (c) Bentheimer sandstone pore throats; (d) Bentheimer sandstone pore bodies with voxel size  $0.0025 \times 0.0025 \times 0.0025$  [ $\text{mm}^3$ ].

distributions (Fig. 13a and b respectively). Note that averaging techniques were applied for results obtained by different segmentation settings used for both (1) the type of connectivity considered for processing adjacent voxels in the matrix, and (2) a contrast factor that was applied to reduce the number of seeds for watershed processing.

The pore body and pore throat diameter maxima are in the range 0.015–0.025 mm. The average pore body diameter is 0.014 mm and pore throat diameter 0.012 mm.

The porosity results from image analysis methods were compared to porosity methods obtained by microscopic inspection, mercury intrusion and capillary flow porometry. To compare the various results, it was necessary to normalize the distribution curves of the other methods from the literature. Fig. 14a and b shows a variation in the pore throat and pore body diameter of the different measuring techniques. The pore throat diameter distribution obtained in this study is in line with the mercury intrusion results that were found in the literature (Halisch, 2013b; Kahl et al., 2013; Maloney et al., 1990). The capillary flow porometry results published by Halisch (2013b) show larger values.

The pore body diameter distribution results are comparable to the pore throat results. Fig. 14b shows that the mercury intrusion technique and its interpretation underestimate the large pore bodies and overestimate the small pore bodies. As the pore bodies can be surrounded by pore throat and smaller pore bodies, the intrusion pressure will be larger/smaller than the real pressure equivalent for certain pores. As a result, this will increase the number of intermediate diameter pores.

Moreover, it is found that small diameter pore bodies tend to be more accurately calculated by micro-CT analysis, larger pore bodies by 2D image analysis, and the largest diameter pore bodies from thin section analysis. Moreover, this variation in pore body size is due to the definition of circle-type cross-sectional results in 2D and voxel-size spherical volume distributions in 3D measurements. Both optical inspection and image analysis tend to estimate pore bodies that are too large (Maloney et al., 1990). Since pore radii

smaller than 0.01 mm can only be reliably determined by mercury porosimetry, and pores with a radius larger than 0.05 mm (the macropore class), are better measured with a combination of thin sections, image analysis and micro-CT techniques, it can be concluded that a combination of different methods is required to determine a realistic image of the pore system.

It should be noted that the micro-CT scan approach provides a direct description of the pore space, but is limited by the machine resolution – a few microns ( $5 \mu\text{m}$ ). The mercury injection method, although able to determine micro- and meso-pores, is a time-consuming technique that contaminates samples with mercury and hydraulically fractures the friable grain framework (Halisch, 2013a).

### 6.2.3. Porosity

In this section the porosity results obtained by Ultra Pycnometer, gravimetric and CT scan measurements are compared.

First, we conducted laboratory measurements to investigate the influence on porosity of wet/dry conditions, and the origins of the sample collection points at the quarry. The obtained data sets (Fig. 15) show porosity with values around 0.248 ( $\pm 0.019$ ). The plotted data shows the extreme values. The results obtained from the old core samples (OS) are lower than those from fresh (FS) and intermediate cores (IS); differences of ca. 7–8 % in porosity for dry conditions (Ultra Pycnometer) and for wet conditions (gravimetric method) were observed. The reduction in the porosity of Bentheimer sandstone can be incorporated to pore clogging with time, as was exhibited in both methods. This restriction and blocking of pore throats can be a result of clay expansion within sandstone matrix. Based on SEM analyses (Fig. 10a–b), the reduction in porosity can be attributed to kaolinite crystals. In addition, the degree of compaction and cementation by hematite and quartz overgrowth on the original beach sand reduces the intergranular pores and decreases permeability by about two orders of magnitude (Sneider, 1987).

We compare laboratory measurements with image analysis and X-ray techniques. All measurement results are presented in Table 2. Porosities measured with the Ultra Pycnometer and gravimetric method give the effective porosity, as only connected pores are included. The laboratory methods gave an average result of 0.248 ( $\pm 0.019$ ); image analysis 0.247, 0.260 and 0.255 with micro-CT scanning and medical-CT scanning respectively. For making comparison more relevant between all the conducted measurements, the small pores obtained from image analysis (diameter smaller than  $2.5 \mu\text{m}$ ) were excluded from the pore distribution due to the resolution of the equipment. As a result, slightly higher (~2%) porosity values obtained by image analysis and X-ray techniques than by laboratory measurements, confirmed that total porosity was determined.

In summary, Bentheimer sandstone presents a high porosity within a range of 0.23–0.27 (average = 0.251). In the case of the samples taken from the same block, the bandwidth decreases significantly, for example, 0.25–0.27 for old, 0.23–0.24 for intermediate samples and 0.25–0.26 (all Ultra Pycnometer method). In general, the measured values were in good agreement (Table 2), with an average deviation for the group of intermediate samples of 4% for the Ultra Pycnometer results, 1% for the gravimetric results, and 9% and 4% for the old and 3% and 1% for fresh samples respectively. It appears from the results that image analysis of random thin sections and CT scans gives comparable results. It should be noted that porosity at reservoir conditions is less than that determined in ambient conditions in the laboratory by analytical methods (98%–80% of porosity in ambient conditions, as confirmed by Selle (2000)).

Comparison of the measured porosity results with data from the literature (Halisch, 2013a; Kemper, 1968; Klov, 2000; Louis et al.,

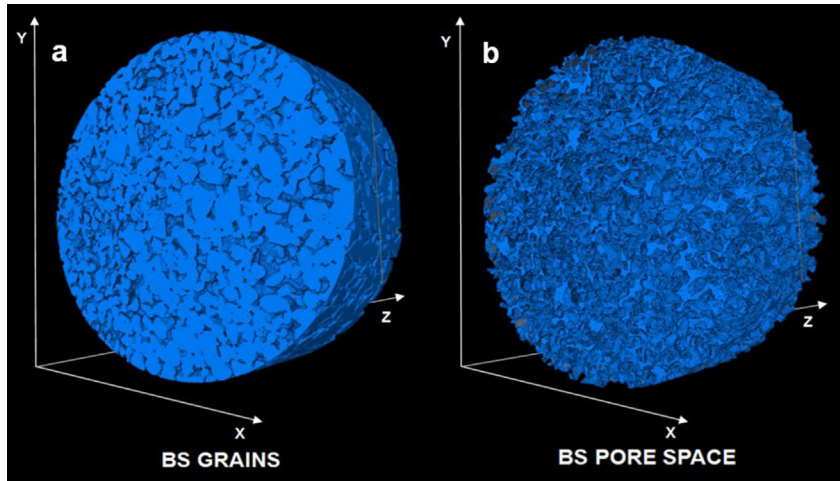


Fig. 12. 3D view of the reconstructed (a) grains and (b) pore space.

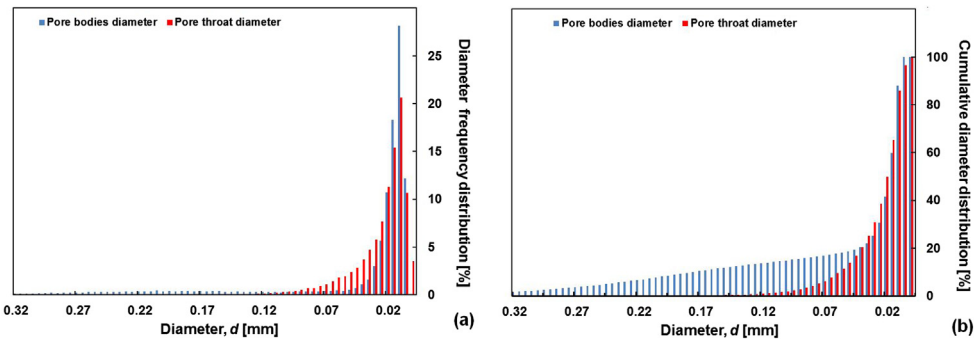


Fig. 13. (a) Pore bodies and throats diameter frequency distribution; (b) Pore bodies and throats cumulative diameter distribution.

2003; Maloney et al., 1990; Van Baaren et al., 1990) shows a good correlation (Table 3). All results are in the range 0.20–0.25. It should be noted that none of the porosity determined by image analysis took into account the presence of clay matrixes.

#### 6.2.4. Grain size distribution and sorting

Grain size distributions of Bentheimer sandstone are plotted for data obtained from stereological measurements of thin sections and Avizo measurements of micro-CT scans. The calculations were done on the two-dimensional data sets obtained from the thin sections images after processing (Fig. 16).

The grain size distributions obtained for 20 thin sections and 10 SEM images and micro-CT scans are plotted as grain diameter size frequency histograms % and grain volume frequency histograms % (Fig. 17a). The volume % conversion has been created with spherical particles. Cumulative frequency distribution curves are constructed for the grain diameter and the grain volume (Fig. 17b). Based on Fig. 17b, the median grain size obtained from thin sections is  $D_{TS50} = 0.235$  mm, 90% of the distribution lies above  $D_{TS90} = 0.180$ , and 10% of the population lies above the  $D_{TS10} = 0.320$  mm. Similarly, for grain diameter distribution obtained from micro-CT scans  $D_{CT50} = 0.320$  mm,  $D_{CT10} = 0.475$  mm,  $D_{CT90} = 0.250$  mm. In addition, a Trask sorting factor of 1.33 was calculated by estimating

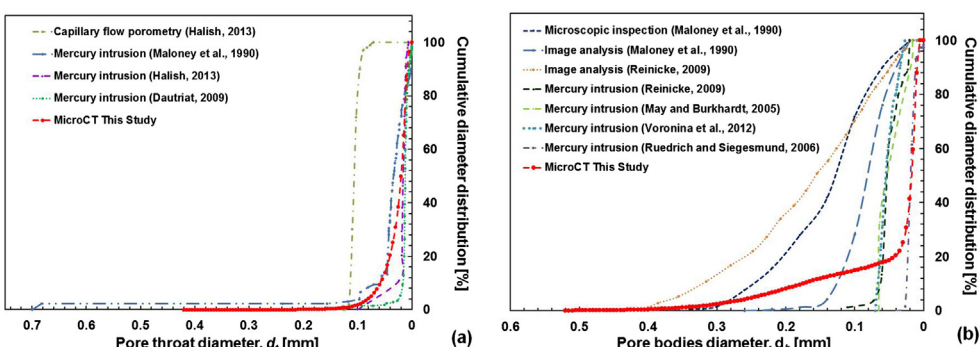
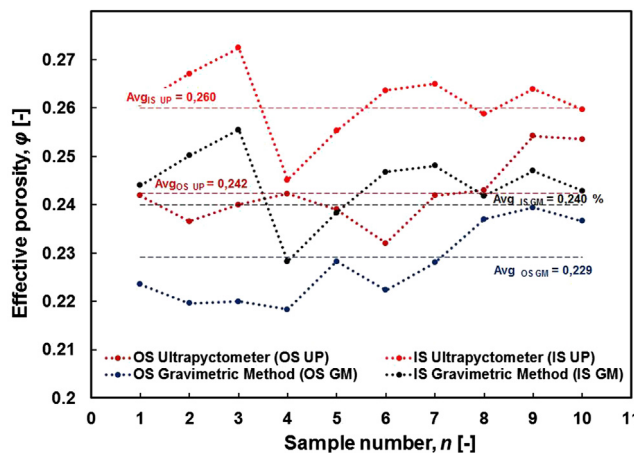


Fig. 14. (a) Comparison of the cumulative pore-throat diameter distributions; (b) Comparison of the cumulative pore-bodies diameter distributions.



**Fig. 15.** Laboratory measurements of porosity of intermediate core samples (IS) and old core samples (OS).

**Table 2**

All porosity results obtained by applying different measurement methods.

Method		Samples type	Average porosity
Laboratory			
	Ultra Pycnometer	OS	$0.242 \pm 0.005$
	Gravimetric methods	OS	$0.229 \pm 0.005$
	Ultra Pycnometer	IS	$0.261 \pm 0.005$
	Gravimetric methods	IS	$0.249 \pm 0.005$
	Ultra Pycnometer	FS	$0.259 \pm 0.005$
	Gravimetric methods	FS	$0.245 \pm 0.005$
	Gravimetric methods	FSQ 1	$0.239 \pm 0.005$
		FSQ 2	$0.257 \pm 0.005$
		FSQ 3	$0.238 \pm 0.005$
		FSQ 4	$0.265 \pm 0.005$
			<b><math>0.248 \pm (0.019)</math></b>
<b>Average from laboratory methods</b>			
Stereology	Image analysis	Thin sections average	0.247
X-ray technique	Micro-CT scanner	Pencil core sample	0.260
X-ray technique	Medical-CT scanner	FS	0.255
<b>Average from imaging methods</b>			<b>0.254</b>

the 1st and 3rd quartiles of the cumulative grain-size distribution (Selley, 2000).

The grain size distribution and degree of sorting are strongly related to the sediments transport and the energy of the depositional environment (Dutton and Willis, 1998). Consequently, we can conclude that determined well sorted Bentheimer grains are a result of the rather constant energy of the waves during transgressive-regressive cycles. The wave velocity was too low to carry the coarser grained sediments.

Comparison of our image/CT scans measurements with data from the literature (Klov, 2000; Maloney et al., 1990; Reinicke, 2009) shows that all the data display similar results (Fig. 18). The median grain size is in the range 0.20–0.33 mm. With respect to the image analysis method used, there were some discrepancies

between the results obtained. Both 2D and 3D image analysis have lower detection boundaries that are set by the size of pixels. In the case of the presented data, the resolutions were 0.58, 10, 68–89, and 2.5 μm for studies by Reinicke (2009), Maloney et al. (1990), Klov (2000) and micro-CT scans respectively. However, the variation of the samples type (different scales) and origin should be as well attributed to the spread in the results. Nevertheless, the magnitudes of the predicted grain size were comparable.

### 6.2.5. Permeability

Absolute gas and liquid permeability, and permeability measured in flow experiments were investigated for the old, intermediate and fresh samples (Table 4). An example of the obtained results for absolute gas permeability is presented in Fig. 19a. For comparison with image analysis methods, the absolute permeability was calculated from the grain size distribution (Table 4) using Carman–Kozeny. In addition, to examine the impact of the geographic location of the sample collection, the flow permeability

was measured for all sample types (OS, IS, FS, FQ1–4). The different methods and all samples results show a close agreement in the range 1.35–3.09 Darcy, with an average of 1.80 Darcy.

It can be seen that the mean values for each type of the measured samples show a good representatives of the values for each original block from which the samples were drilled ( $OS_{Ave} = 1.53 \pm 0.14$  Darcy,  $IS_{Ave} = 2.89 \pm 0.14$  Darcy,  $FS_{Ave} = 2.78 \pm 0.19$  Darcy). The four measurement methods used for all sample types show consistency in the trend of obtained values. In other words, from the highest to the lowest values respectively; the Ruska gas permeability; the Ruska liquid permeability; liquid permeability measured flow experiments and permeability obtained from stereological measurements. The permeability values obtained for intermediate and fresh samples show close agreement, however, the results on the old

**Table 3**  
Bentheimer sandstone porosity data gathered from literature.

Method	Porosity
Mercury porosimeter (Dautriat et al., 2009)	0.240
Mercury porosimeter (Klov, 2000)	0.213–0.226
Mercury porosimeter (Halisch, 2013a)	0.200–0.230
Thresholded Gaussian Fields (Thovert and Adler, 2011)	0.230
Optical porosity (Klov, 2000)	0.202–0.227
Visual observation (Andrew et al., 2013b)	0.220
Visual observation (Blunt et al., 2013)	0.200
Gravimetric method (Louis et al., 2003)	0.245
Boyl's law expansion technique (Fired sample) (Maloney et al., 1990)	0.247

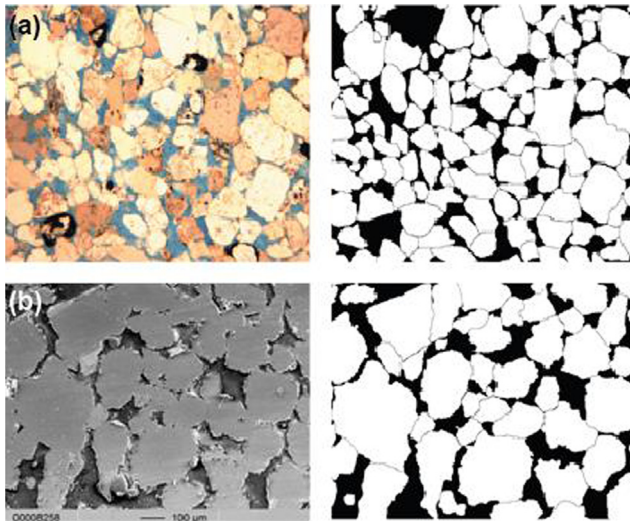


**Fig. 16.** 2D images of a Bentheimer sandstone sample obtained by: (a) optical microscopy on polished sections; and (b) SEM. On the left side are the original images and on the right binary segmented images, where the matrix is represented by black patterns and the pore space and grain contacts by white patterns. The porosity measurements were done on images with absence of grain contact determination.

samples are lower. The old samples have been measured again following the original measurement method. As a result the original measurements show higher values (35%). This reduction in permeability with the old samples can be attributed to pore clogging with and possible volume increase by hydroxylation of fines.

The spread of the values obtained from four different blocks with locations is visualized in Table 4 ( $FQ_{Ave} = 1.54 \pm 0.52$ ). It can be concluded that the values depend on both the time when the samples were obtained and the location of the blocks in the quarry. As in the case of porosity the block homogeneity is clearly visible.

Fig. 19b shows the relationship between the Ultra Pycnometer porosity and gas permeability of the old, intermediate and fresh samples; the permeability increases log-linearly with the porosity. As the quarry samples are investigated a linear relation between porosity and permeability is observed what is the characteristic feature mainly of the shallow buried parts. With increasing the buried depth, diagenetic alterations reduce the permeability relatively more than the porosity what would result in a power function relation.

Comparison of our results with the literature data shows close agreement of the absolute permeability (Table 5).

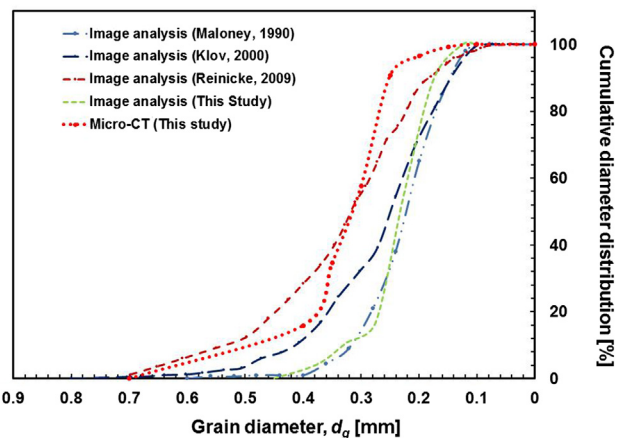


**Fig. 18.** Comparison of cumulative grain size distribution obtained in various studies with values determined in this study.

#### 6.2.6. Mechanical behavior

The dry and water-saturated Bentheimer sandstone samples were subjected to monotonic loading and alternating loading (the unloading and reloading). The elastic constants of Bentheimer sandstone exhibit different characteristics for different scenarios. The axial compressive strength and elastic constants of dry and water saturated sandstones under monotonic loading and alternating loading are listed in Table 6. Tests result in the smaller tangent modulus for monotonic loading than for alternating loading. Elastic modulus of water-saturated Bentheimer sandstone is smaller than that of dry sandstone at the same strain rate, although the difference between Poisson ratios of dry and water-saturated sandstones is insignificant. The Poisson ratio of dry samples is slightly smaller than of water-saturated samples. The wetting softening behavior of Bentheimer sandstone can be expressed by softening coefficient – ratio of the axial compressive strength of water saturated sandstone and the axial compressive strength of dry sandstone. Based on the experiments the softening coefficients of Bentheimer sandstone is 87.3%. The determined slight strength reduction is related to existence of pore fluid, fluctuations in the physical state and as a result to a decrease in the bonding strength of the rock matrix while wetting (Lin et al., 2005).

The measured values represent mechanical stability of the Bentheimer sandstone and are a result of quartz rich composition and the good sorting. Quartz does not exhibit twinning and cleavages, and are reflected to be stiff (Mansurbeg, 2001).

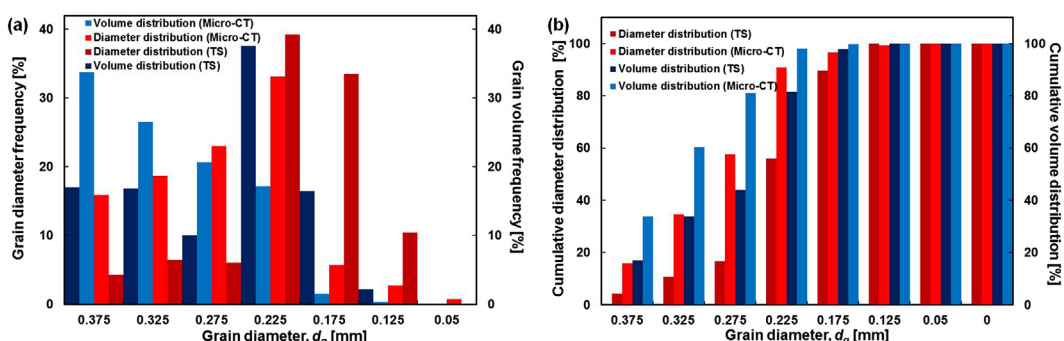


**Fig. 17.** (a) Grain size frequency histograms and grain volume frequency histograms obtained from statistical reconstruction of 2D thin sections of Bentheimer sandstone; (b) Cumulative percent frequency distribution of diameter curve and cumulative percent frequency distribution of volume curve.

**Table 4**

Bentheimer sandstone permeability data obtained by various methods, per sample and per block. Number of measurements per block and per method is  $n = 10$ .

Method for each block	Samples type	Average permeability [D]	Average permeability for all methods [D]
Ruska gas permeameter	Old core samples	$1.74 \pm 0.07$	$1.53 \pm 0.14$
Liquid permeameter		$1.51 \pm 0.10$	
Flow experiment		$1.67 \pm 0.05$	
Grain size distribution from thin sections (Carmen–Kozeny)		$1.45 \pm 0.12$	
Ruska gas permeameter	Intermediate core samples	$3.02 \pm 0.17$	$2.89 \pm 0.14$
Liquid permeameter		$2.87 \pm 0.18$	
Flow experiment		$2.98 \pm 0.04$	
Grain size distribution from thin sections (Carmen –Kozeny)		$2.70 \pm 0.15$	
Ruska gas permeameter	Fresh samples	$2.98 \pm 0.17$	$2.78 \pm 0.19$
Liquid permeameter		$2.68 \pm 0.12$	
Flow experiment		$2.90 \pm 0.07$	
Grain size distribution from thin sections (Carmen–Kozeny)		$2.56 \pm 0.10$	
Flow experiment	Quarry samples 1	$1.48 \pm 0.04$	—
	Quarry samples 2	$1.04 \pm 0.03$	
	Quarry samples 3	$2.27 \pm 0.09$	
	Quarry samples 4	$1.35 \pm 0.04$	

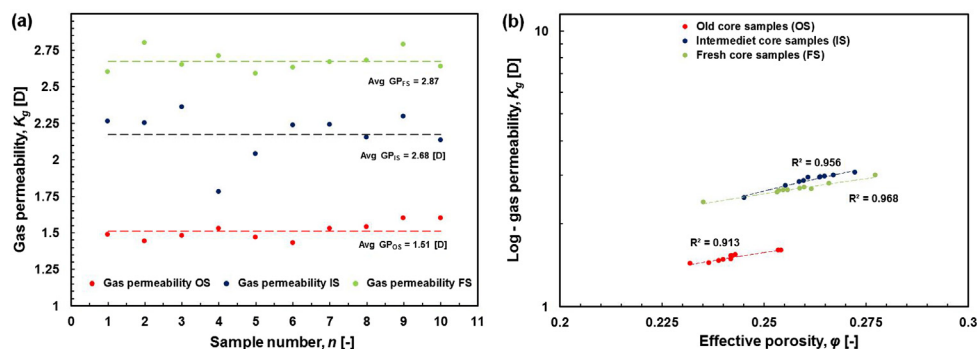


Fig. 19. (a) Laboratory measurements of gas permeability of old (OS) and intermediate (IS) core samples;(b) Por/Perm cross-plot for Bentheimer old and fresh cores analysis. Porosity was measured with the Ultra Pycnometer and permeability with a Ruska gas permeameter.

#### 6.2.7. Specific surface charge area

The adsorption and desorption isotherm has been obtained by measuring the amount of nitrogen adsorbed and desorbed across a range of pressure steps at a constant temperature of 77 K (Fig. 20a). The three samples (S1–S3) show adsorption/desorption hysteresis that fits with a Type III isotherm of the Brunauer classification. The presence of very narrow hysteresis – adsorption and desorption branches – that almost coincide indicates the lack of structural heterogeneity of Bentheimer sandstone and percolation. The capillary condensation region is recognized to be above a relative pressure of 0.4. The phenomenon of capillary condensation is an effect of the difference in the filling and emptying mechanisms of the mesopores (2–50 nm in accordance with the IUPAC Pore Size Classification Scheme (Sing et al., 2008)), giving rise to a hysteresis loop between adsorption and desorption. Specifically, at low relative pressures, coverage occurs first on a monolayer, followed by the next layers. Further, the capillary condensation occurs at the adsorbed film, which acts as a nucleus.

Applying the BET equation to the part of the adsorption isotherms corresponding to relative pressures in the range of 0.16 and 0.24 (where capillary condensation does not occur), we obtain a surface area equal to  $0.45 \text{ m}^2/\text{g}$  (Fig. 20b). The above value is in accordance with those reported by Halisch (2013a).

#### 6.2.8. Dielectric behavior

The dielectric behavior of Bentheimer sandstone is evaluated based on the change in surface charge due to the change in pH of the solution. Fig. 21 shows the surface charge,  $\delta_0$ , and proton balance related to the dissolution effects. The differences in the acid/base consumption balance are used to calculate the surface charge (from the slope of the graph) and acid/base consumption for sample dissolution (assumption – the solution is saturated with dissolved sample matter (e.g. sample impurities or sample matter itself) for the smallest sample mass used in this plot).

The point of zero charge (PZC) value for the Bentheimer sandstone surface indicates that, at pH values higher than 8, the surface

**Table 5**

Bentheimer sandstone permeability data gathered from literature.

Method	Absolute permeability [Darcy]
Perimeter (Ersland et al., 2010)	1.10
Perimeter (Dautriat et al., 2009)	1.60
Gas perimeter (Klinkenberg permeabilities) (Halisch, 2013a)	0.52–0.69
Gas perimeter (fired samples) (Maloney et al., 1990)	2.39
Water flow experiments	2.37
Water flow experiments	1.41

**Table 6**  
Stress/strain measurements.

Samples	Max stress $\sigma_{\max}$ [MPa]	Loading type			
		Monotonic load		Alternating load	
		E-module tangent 50% $E_t$ [GPa]	Poisson ratio $\nu$	E-module tangent 50% $E_t$ [GPa]	Poisson ratio $\nu$
5 BS dry cores	38.93	14.69	0.25	18.38	0.22
5 BS water -saturated cores	33.99	13.52	0.28	17.72	0.25

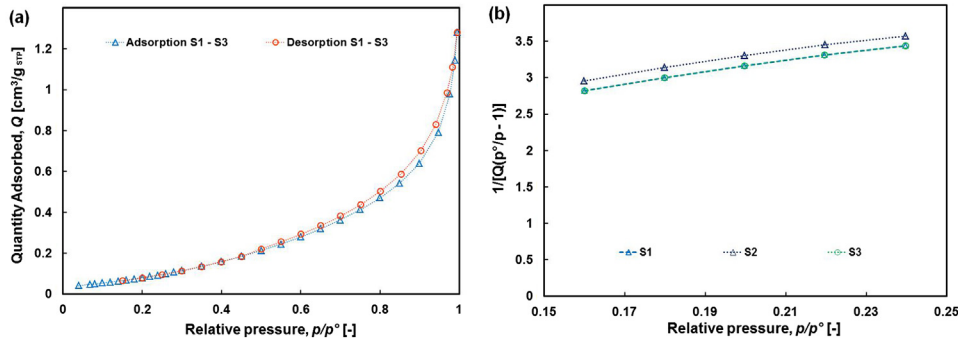


**Fig. 20.** (a) An isotherm linear plot, representing the relation between the quantity adsorbed and the equilibrium pressure of the nitrogen (at constant temperature  $-77$  K); (b) Example of a BET plot.

becomes negatively charged and the electrostatic repulsion of clays occurs. A similar phenomenon was observed in the clay dispersion and release studies of Gray and Rex (1966) and Simon (1976). Clay particles were probably distributed in the sample and became mobile in contact with pH > 8 fluid. The higher the pH, the more visible the effect is. These effects may reduce the permeability of

the rock. In addition, the effect of the presence of goethite and hematite in the samples on the point of zero charge was noted. Iron oxides represent point of zero charge in the range of 8.5–11 (Appel et al., 2003). The value of point of zero charge measured in this study differs from value observed by Farooq et al. (2011) by zeta potential determination of Bentheimer in water and different electrolytic solutions. Further work on this topic is not within the scope of this study. It is suggested that the sandstone be fired to glass before performing dielectrical experiments (Shaw et al., 1991).

## 7. Conclusions

In this paper we determined the properties of Bentheimer sandstone for petrophysical, petrological behavior and dielectrical impurities, especially for multiphase flow studies. Additionally, we estimated a variation in the accuracy of predictions of the sandstone properties based on theoretical and experimental estimations of the grain and pore size distribution. The results have been compared to our own laboratory and literature data. After the results were gathered and analyzed, they show a spread in values that can be summarized as follows:

- Bentheimer sandstone is easy obtainable, well sorted porous material for comparative non-conductive physical experiments and preparing 3D pore frameworks for theoretical studies. The presence of accessory clay and (hydr)oxides makes it less favorable for conductive behavior;
- Bentheimer sandstone shows a constant mineralogy over investigated samples, predominantly consisting of monocrystalline detrital quartz with authigenic quartz overgrowths. The high quartz content results in a high mechanical stability what was proven by the uniaxial compressive test. However, the variety of accessory minerals in the Bentheimer sandstone (feldspars, clays, iron oxides and carbonate minerals) might lower in a smaller extend its chemical and mechanical stability. For example, as a result of the interaction of the sandstone with electrolytes, random dissolution of heterogeneous K-feldspars and precipitation of clays occurred and occurs (softening coefficient of Bentheimer is 87.3%). However, the small amounts of

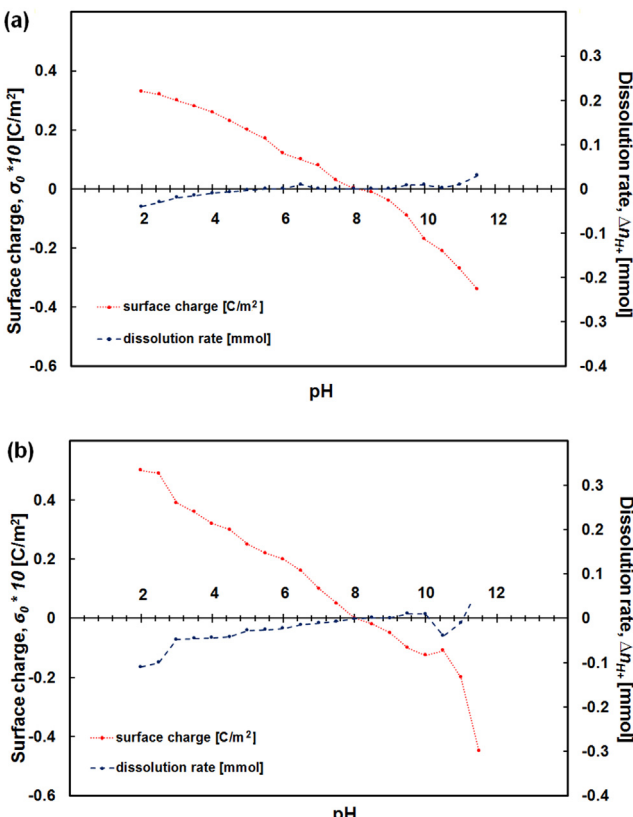


**Fig. 21.** Surface charge density  $\sigma_0$  and sample dissolution effect  $\Delta n_{H^+}$  for Bentheimer sandstone in (a) de-ionized water; (b) 2.2M NaCl solution. Temperature is 21 °C.

K-feldspar did not produce enough of these secondary clays to significantly affect the bulk reservoir porosity and permeability, unless a migration of clays created a proportionally large clogging zone, which incidentally happens;

- The sandstone presents high porosity in the range 0.23–0.27. The porosity values obtained by high-resolution microtomography or thin sections were slightly lower than those found in laboratory measurements. This can be due to pixel resolution, because some of the smaller pores (pixel level) are merged with the matrix and not visible. However, the pore space information obtained using microtomography or thin sections is shown to be sufficient for spatial sample characterization. Combining all the approaches to porosity determination gives a better estimation of the pore space (body and throat distribution, specific pore space, specific surface, etc.) and ultimately provides a more detailed description, covering a wider range of pore sizes from microns to mm (sizes varying by more than three orders of magnitude);
- As a result of depositional environment, Bentheimer sandstone is composed of well sorted mostly rounded to sub-rounded grains. It shows a regular and narrow distribution of pore sizes (~10–50 µm diameter of pore throats), which results in a high permeability. In addition, narrow band in its grain size distribution and specific surface area make Bentheimer sandstone to be candidate for a reference rock for laboratory studies;
- The repeatability of the experimental results is high, both in our work and compared to literature studies, i.e., porosity ( $\varphi$ ) is 0.200–0.260, the median grain diameter lies in the range 0.20–0.33 mm, the median pore throat and bodies diameters are 0.01–0.12 mm and 0.02–0.18 mm respectively;
- Surface charge problems due to the occurrence of dispersed accessory, i.e., iron (hydr)oxides and clay mineral, have been observed. It is suggested that the sandstone be fired to glass before performing dielectrical experiments.

By comparing different techniques to measure certain parameters, we conclude that the efficiency and accuracy of the various techniques must be taken into consideration when planning the measurements, even though the difference between the obtained values remains relatively low. It should be noted that it was not possible to eliminate natural variation of the samples for all measurements, mainly because of different types of samples needed for certain tests. The variations can be concluded as follows:

- Porosity measurements – Ultra Pycnometer measurements with gas give higher values than gravimetric methods (4–5% difference). Using N<sub>2</sub> or He gas instead of water has the advantage of being non-reactive (important when samples contain more clays). Image analysis gives results close to the average values obtained by laboratory methods;
- Permeability measurements: gas measurements show higher results than water permeability and can increase with increasing pore pressure. The water permeability values can be estimated based on gas permeability measurements;
- Pore bodies and throat distribution: the most appropriate method to measure the small diameter pore bodies are micro-CT analysis (discrete result) and mercury porosimetry (bulk result) for pore radii smaller than 0.01 mm. The larger pore bodies and pores with a radius larger than 0.05 mm are more accurately measured with a combination of thin sections, image analysis and micro-CT. The assumption that isotropy and block – scale homogeneity are present in the entire matrix means that the results are assumed to be realistic. Hence, a combination of

different methods provides a representative image of the pore system through different scales;

- Grain size distribution: both 2D and 3D image analysis have smaller values due to the pixel size measurements. The orders of magnitude of the grain size distribution results for the 2D and 3D methods were comparable.

## Acknowledgments

The authors want to thank the CATO program – the Dutch national research program on CO<sub>2</sub> Capture and Storage for financial support of the study, and Karel Heller, Arno Mulder, Joost van Meel for their contributions to the experimental work and fruitful discussions. The special thanks to Koenraad Elewaut – the substance of the paper benefited from his comments and discussions with him. Further we acknowledged staff of the Romberg Quarry in Gildehaus for their assistance in the quarry.

## References

- Al-Futaisi, A., Patzek, T.W., 2004. Impact of microscopic NAPL-water interface configurations on subsequent gas injection into water-wet permeable rocks. *Dev. Water Sci.* 1, 139–151.
- Al-Menhal, A., Reynolds, C., Lai, P., Niu, B., Nicholls, N., Crawshaw, J., Krevor, S., 2014. Advanced reservoir characterization for CO<sub>2</sub> storage. In: Paper Presented at the IPTC 2014: International Petroleum Technology Conference, December, 10–12, 2014.
- Al-Muntasher, G.A., Zitha, L.J., Nasr-El-Din, H.A., 2010. A new organic gel system for water control: a computed tomography study. *SPE J.* 15, 197–207. <http://dx.doi.org/10.2118/129659-PA>.
- Al Ghamdi, T.M., Arns, C.H., 2012. Predicting Relative Permeability from NMR Relaxation-diffusion Responses Utilizing High Resolution Micro X Ray-CT Images.
- Amro, V.M., Kessel, D., 1996. Feasibility of microbially improved oil recovery (MIOR) in northern German oil reservoirs. *Erdoel Erdgas Kohle* 112, 193–195.
- Andersson, L., Herring, A.L., Newell, D.L., Carey, B., 2013. Wildenschild D high-resolution X-ray tomography imaging of supercritical CO<sub>2</sub>: investigating capillary trapping under reservoir conditions and addressing wettability alteration. In: AGU Fall Meeting Abstracts, p. 03P.
- Andrew, M., Bijeljic, B., Blunt, M.J., 2013a. Pore scale imaging of geological carbon dioxide storage under in situ conditions. *Geophys. Res. Lett.* 40, 3915–3918.
- Andrew, M., Bijeljic, B., Blunt, M.J., 2013b. Reservoir-condition pore-scale imaging of supercritical carbon dioxide. In: Paper Presented at the SPE Annual Technical Conference and Exhibition, New Orleans, Louisiana, USA.
- Appel, C., Ma, L.Q., Dean Rhue, R., Kennelley, E., 2003. Point of zero charge determination in soils and minerals via traditional methods and detection of electroacoustic mobility. *Geoderma* 113, 77–93. [http://dx.doi.org/10.1016/S0016-7061\(02\)00316-6](http://dx.doi.org/10.1016/S0016-7061(02)00316-6).
- Bakke, S., Øren, P.E., 2013. 3-D pore-scale modelling of sandstones and flow simulations in the pore networks. *SPE J.* 2, 136–149. <http://dx.doi.org/10.2118/35479-pa>.
- Berg, C.F., 2012. Re-examining Archie's law: conductance description by tortuosity and constriction. *Phys. Rev. E Stat. Nonlinear Soft Matter Phys.* 86 <http://dx.doi.org/10.1103/PhysRevE.86.046314>, 046314/046311–046314/046319.
- Betz, D., Führer, F., Greiner, G., Plein, E., 1987. Evolution of the lower Saxony basin. *Tectonophysics* 137, 127–170.
- Blöcher, G., Reinsch, T., Hassanzadegan, A., Milsch, H., Zimmermann, G., 2014. Direct and indirect laboratory measurements of poroelastic properties of two consolidated sandstones. *Int. J. Rock Mech. Min. Sci.* 67, 191–201. <http://dx.doi.org/10.1016/j.ijrmms.2013.08.033>.
- Blunt, M.J., et al., 2013. Pore-scale imaging and modelling. *Adv. Water Resour.* 51, 197–216. <http://dx.doi.org/10.1016/j.advwatres.2012.03.003>.
- Borschinsky, R., Kulke, H., 1992. Facies model of an oil reservoir using three-dimensional modeling: example Bentheimer sandstone, field Georgsdorf (north-eastern Part), Germany. *Erdoel Erdgas Kohle* 108, 442–447.
- Brunauer, S., Emmett, P.H., Teller, E., 1938. Adsorption of gases in multimolecular layers. *J. Am. Chem. Soc.* 60, 309–319. <http://dx.doi.org/10.1021/ja01269a023>.
- Bultreys, T., De Boever, W., Brabant, L., Cnudde, V., 2013. Comparison of pore network models for the investigation of fluid flow properties in building stones. In: Paper presented at the 5th International Conference on Porous Media & Annual Meeting of the International Society for Porous Media (InterPore 2013), May, 22–24, 2013.
- Calvo, J.I., Hernández, A., Prádanos, P., Tejerina, F., 1996. Charge adsorption and zeta potential in cycloporine membranes. *J. Colloid Interface Sci.* 181, 399–412. <http://dx.doi.org/10.1006/jcis.1996.0397>.
- Chandler, M.A., Kocurek, G., Goggin, D.J., Lake, L.W., 1989. Effects of stratigraphic heterogeneity on permeability in eolian sandstone sequence, page sandstone, northern Arizona. *AAPG Bull. Am. Assoc. Pet. Geol.* 73, 658–668.

- Clavaud, J.-B., Maineult, A., Zamora, M., Rasolofosaon, P., Schlitter, C., 2008. Permeability anisotropy and its relations with porous medium structure. *J. Geophys. Res. Solid Earth* 113, B01202. <http://dx.doi.org/10.1029/2007jb005004>.
- Dautriat, J., Gland, N., Guelard, J., Dimanov, A., Raphanel, J.L., 2009. Axial and radial permeability evolutions of compressed sandstones: end effects and shear-band induced permeability anisotropy. In: Vinciguerra, S., Bernabé, Y. (Eds.), Rock Physics and Natural Hazards. Pageoph Topical Volumes. Birkhäuser Basel, Germany, pp. 1037–1061. [http://dx.doi.org/10.1007/978-3-0346-0122-1\\_14](http://dx.doi.org/10.1007/978-3-0346-0122-1_14).
- De Boever, W., Bultreys, T., Traska, M., Mock, A., Brabant, L., Cnudde, V., 2013. 3D characterisation of the Bentheimer Sandstone and Euville Limestone, in relation to fluid flow through their pore networks. In: Paper presented at the 14th Euroseminar on Microscopy Applied to Building Materials (EMABM 2013), June, 10–14, 2013.
- De Jager, J., Geluk, M.C., 2007. Petroleum geology. In: Wong, T.E., Batjes, D.A.J., De Jager, J. (Eds.), *Geology of the Netherlands*. Royal Netherlands Academy of Arts and Sciences, Amsterdam, pp. 241–264.
- Doughty, D.A., Tomutsa, L., 1996. Multinuclear NMR microscopy of two-phase fluid systems in porous rock. *Magn. Reson. Imag.* 14, 869–873.
- Dresen, G., Stanchits, S., Rybacki, E., 2010. Borehole breakout evolution through acoustic emission location analysis. *Int. J. Rock Mech. Min. Sci.* 47, 426–435. <http://dx.doi.org/10.1016/j.ijrmms.2009.12.010>.
- Dubelaar, W.C., Nijland, T.G., 2015. The Bentheim Sandstone: geology, petrophysics, varieties and its use as dimension stone. In: Lollino, G., Giordan, D., Maranteau, C., Christaras, B., Yoshinori, I., Margottini, C. (Eds.), *Engineering Geology for Society and Territory*, vol. 8. Springer International Publishing, Switzerland, pp. 557–563. [http://dx.doi.org/10.1007/978-3-319-09408-3\\_100](http://dx.doi.org/10.1007/978-3-319-09408-3_100).
- Dutton, S.P., Willis, B.J., 1998. Comparison of outcrop and subsurface sandstone permeability distribution, lower cretaceous Fall River formation, South Dakota and Wyoming. *J. Sediment. Res.* 68, 890–900. <http://dx.doi.org/10.2110/jsr.68.890>.
- Ersland, G., Husebø, J., Graue, A., Baldwin, B.A., Howard, J., Stevens, J., 2010. Measuring gas hydrate formation and exchange with CO<sub>2</sub> in Bentheim sandstone using MRI tomography. *Chem. Eng. J.* 158, 25–31.
- Farooq, U., Tweheyo, M.T., Sjøblom, J., Øye, G., 2011. Surface characterization of model, outcrop, and reservoir samples in low salinity aqueous solutions. *J. Dispers. Sci. Technol.* 32, 519–531.
- Feali, M., et al., 2012. Qualitative and quantitative analyses of the three-phase distribution of oil, water, and gas in Bentheimer sandstone by use of micro-CT imaging. *SPE Reserv. Eval. Eng.* 15, 706–711. <http://dx.doi.org/10.2118/151609-pa>.
- Fernø, M.A., Haugen, Å., Wickramathilaka, S., Howard, J., Graue, A., Mason, G., Morrow, N.R., 2013. Magnetic resonance imaging of the development of fronts during spontaneous imbibition. *J. Pet. Sci. Eng.* 101, 1–11. <http://dx.doi.org/10.1016/j.petrol.2012.11.012>.
- Fodisch, H., Wegner, J., Hincapie-Reina, R., Ganzer, L., 2013. Characterization of glass filter micromodels used for polymer EOR flooding experiments. *DGMK Tagungsbericht 2013–1*, 325–334.
- Frette, O.I., Helland, J.O., 2010. A semi-analytical model for computation of capillary entry pressures and fluid configurations in uniformly-wet pore spaces from 2D rock images. *Adv. Water Resour.* 33, 846–866. <http://dx.doi.org/10.1016/j.advwatres.2010.05.002>.
- Fuchtbauer, H., 1963. Excursion guide book I: paleogeography and reservoir properties of the lower cretaceous Bentheim sandstone. In: 6th World Petroleum Congress, Hannover, pp. 42–43.
- Fuchtbauer, H., 1955. Zur Petrographie des Bentheimer Sandsteins im Emsland. Erdöl Kohle 8, 616–617.
- Gray, D., Rex, R., 1966. Formation damage in sandstones caused by clay dispersion and migration. In: Proc., pp. 355–365.
- Gubbins, K.E., 2009. Hysteresis Phenomena in Mesoporous Materials (Dissertation). Universität Leipzig, Leipzig, Germany.
- Halisch, M., 2013a. Application and Assessment of the Lattice Boltzmann Method for Fluid Flow Modeling in Porous Rocks (Dissertation). Technische Universität Berlin, Berlin, Germany.
- Halisch, M., 2013b. Assesment of porous rocks by Capillary flow porometry. In: Paper presented at the International Symposium of the Society of Core Analysts, Napa Valley, California, USA, 2013.
- Hansen, E.W., Stocker, M., Olafsen, K., Kvernberg, P.O., 1999. Gelation kinetics of polymers confined in water/oil-saturated porous materials probed by NMR. *J. Dispers. Sci. Technol.* 20, 723–741. <http://dx.doi.org/10.1080/01932699908943817>.
- Hassan, S., 2012. Electric properties and its effect on microporosity rocks. In: Paper presented at the SPE International Production and Operations Conference & Exhibition, Doha, Qatar, 14–16 May 2012.
- Herring, A.L., 2012. Saturation, Morphology, and Topology of Nonwetting Phase Fluid in Bentheimer Sandstone: Application to Geologic Sequestration of Supercritical CO<sub>2</sub> (Dissertation). Oregon State University.
- Hesselink, F.T., Faber, M.J., 1981. Polymer-surfactant interaction and its effect on the mobilization of capillary-trapped oil. *Surf. Phenom. Enhanc. Oil Recovery* 861–869.
- Hinze, C., 1988. Geologische Karte von Niedersachsen 1: 25.000 Erläuterungen zu Blatt.
- Holt, T., Jensen, J.I., Lindeberg, E., 1995. Underground storage of CO<sub>2</sub> in aquifers and oil reservoirs. *Energy Convers. Manag.* 36, 535–538. [http://dx.doi.org/10.1016/0196-8904\(95\)00061-H](http://dx.doi.org/10.1016/0196-8904(95)00061-H).
- Jacquey, A.B., Cacace, M., Blöcher, G., Huenges, E., Scheck-Wenderoth, M., 2014a. Hydro-mechanical evolution of transport properties in porous media: constrains for numerical modeling of geothermal systems. In: Paper presented at the 3rd European Geothermal Workshop, Karlsruhe, Germany, October, 15–16, 2014.
- Jacquey, A.B., Cacace, M., Blöcher, G., 2014b. Scheck-Wenderoth M modelling of fractured reservoirs: fluid-rock interactions within fault domains. In: GeoMod Potsdam, 31.08.–05.09. 2014, p. 407.
- Jeremiah, J.M., Duxbury, S., Rawson, P.F., 2010. Lower Cretaceous of the southern North Sea Basins: reservoir distribution within a sequence stratigraphic framework. *Geol. Mijnb.* 89, 203–236.
- Johns, M.L., Sederman, A.J., Gladden, L.F., Wilson, A., Davies, S., 2003. Using NMR techniques to probe permeability reduction in rock cores. *AIChE J.* 49, 1076–1084. <http://dx.doi.org/10.1002/aic.690490503>.
- Kahl, W.A., Feeser, V., Hinkes, R., Holzheid, A., Raphanel, J.L., 2013. Anisotropy of Elastic Waves in Sandstone: Correlation with Microstructural Observations. *Geophysical Research Abstracts* 15.
- Kemper, E., 1968. *Geologischer Führer durch die Grafschaft Bentheim und die angrenzenden Gebiete*. Verlag Heimatverein der Grafschaft Bentheim, Nordhorn, Germany.
- Kemper, E., 1976. *Geologischer Führer durch die Grafschaft Bentheim und die angrenzenden Gebiete: mit einem Abriß der emsländischen Unterkreide*. Heimatverein der Grafschaft Bentheim, Bad Bentheim, Germany.
- Kemper, E., van der Burgh, J., 1992. Die tiefe Unterkreide im Vechte-Dinkel-Gebiet: westliches niedersächsisches Becken. *Stichting Het Staringmonument te Losser, Losser, Germany*.
- Klein, E., Baud, P., Reuschlé, T., Wong, T.F., 2001. Mechanical behaviour and failure mode of Bentheim sandstone under triaxial compression. *Phys. Chem. Earth Pt A* 26, 21–25. [http://dx.doi.org/10.1016/S1464-1895\(01\)00017-5](http://dx.doi.org/10.1016/S1464-1895(01)00017-5).
- Klein, E., Reuschlé, T., 2003. A model for the mechanical behaviour of Bentheim Sandstone in the brittle regime. In: Kümpel, H.-J. (Ed.), *Thermo-hydro-mechanical Coupling in Fractured Rock*. Pageoph Topical Volumes. Birkhäuser Basel, pp. 833–849. [http://dx.doi.org/10.1007/978-3-0348-8083-1\\_3](http://dx.doi.org/10.1007/978-3-0348-8083-1_3).
- Klov, T., 2000. *High-velocity Flow in Fractures* (Dissertation). Norwegian University of Science and Technology, Trondheim, Norway.
- Knaap, W., Coenen, M., 1987. Exploration for oil and natural gas. In: Visser, W., Zonneveld, J., Van Loon, A. (Eds.), *Seventy-five Years of Geology and Mining in the Netherlands (1912–1987)*. Royal Geological and Mining Society of the Netherlands, Den Haag, pp. 207–242.
- Kvamme, B., Graue, A., Buanes, T., Kuznetsova, T., Ersland, G., 2007. Storage of CO<sub>2</sub> in natural gas hydrate reservoirs and the effect of hydrate as an extra sealing in cold aquifers. *Int. J. Greenh. Gas Control* 1, 236–246. [http://dx.doi.org/10.1016/S1750-5836\(06\)00002-8](http://dx.doi.org/10.1016/S1750-5836(06)00002-8).
- Kvamme, B., Graue, A., Buanes, T., Kuznetsova, T., Ersland, G., 2009. Effects of solid surfaces on hydrate kinetics and stability. *Geol. Soc. Spec. Publ.* 319, 131–144. <http://dx.doi.org/10.1144/sp319.11>.
- Kvamme, B., Graue, A., Kuznetsova, T., Buanes, T., Ersland, G., 2006. Energy from natural gas hydrate combined with reservoir storage of CO<sub>2</sub>. *WSEAS Trans. Environ. Dev.* 2, 699–710.
- Lin, M.L., Jeng, F.S., Tsai, L.S., Huang, T.H., 2005. Wetting weakening of tertiary sandstones – microscopic mechanism. *Environ. Geol.* 48, 265–275.
- Louis, L., David, C., Metz, V., Robion, P., Menéndez, B., Kissel, C., 2005. Microstructural control on the anisotropy of elastic and transport properties in undeformed sandstones. *Int. J. Rock Mech. Min. Sci.* 42, 911–923. <http://dx.doi.org/10.1016/j.ijrmms.2005.05.004>.
- Louis, L., David, C., Robion, P., 2003. Comparison of the anisotropic behaviour of undeformed sandstones under dry and saturated conditions. *Tectonophysics* 370, 193–212.
- Maldal, T., Gulbrandsen, A.H., Gilje, E., 1997. Correlation of capillary number curves and remaining oil saturations for reservoir and model sandstones. *In Situ* 21, 239–269.
- Maldal, T., Hoiland, H., 1997. Phase behavior and chemical flooding properties of water-oil-nonionic amphiphile mixtures. *In Situ* 21, 271–295.
- Malmborg, P., 2002. Correlation between Diagenesis and Sedimentary Facies of the Bentheim Sandstone, the Schonebeek Field, The Netherlands: Petrographic and Sedimentological Re-evaluation of a Petroleum Reservoir (Master thesis). Lunds Universitet, Lund, Sweden.
- Maloney, D.R., Honarpour, M.M., Brinkmeyer, A.D.I.I.T., 1990. The Effects of Rock Characteristics on Relative Permeability. National Institute for Petroleum, Research Institute Department of Energy, United States.
- Mansfield, P., Bowtell, R., Blackband, S., Guilfoyle, D.N., 1992. Magnetic resonance imaging: applications of novel methods in studies of porous media. *Magn. Reson. Imag.* 10, 741–746.
- Mansfield, P., Issa, B., 1994. Studies of fluid transport in porous rocks by echo-planar MRI. *Magn. Reson. Imag.* 12, 275–278.
- Mansfield, P., Issa, B., 1996. A microscopic model of fluid transport in porous rocks. *Magn. Reson. Imag.* 14, 711–714.
- Mansurbeg, H., 2001. *Modelling of Reservoir Quality in Quartz-rich Sandstones of the Lower Cretaceous Bentheim Sandstones, Lower Saxony Basin, NW Germany* (Dissertation). Lunds Universitet, Lund, Sweden.
- Mayr, S.I., Burkhardt, H., 2006. Ultrasonic properties of sedimentary rocks: effect of pressure, saturation, frequency and microcracks. *Geophys. J. Int.* 164, 246–258. <http://dx.doi.org/10.1111/j.1365-246X.2005.02826.x>.
- McLendon, W.J., et al., 2014. Assessment of CO<sub>2</sub>-soluble non-ionic surfactants for mobility reduction using mobility measurements and CT imaging. *J. Pet. Sci. Eng.* 119, 196–209. <http://dx.doi.org/10.1016/j.petrol.2014.05.010>.

- McLendon, W.J., et al., 2012. Assessment of CO<sub>2</sub>-soluble surfactants for mobility reduction using mobility measurements and CT imaging. In: Paper presented at the 18th SPE Improved Oil Recovery Symposium, Tulsa, OK, United States, April 14–18, 2012.
- Milsch, H., Blöcher, G., 2013. Direct and simultaneous measurements of sandstone porosity, permeability, and electrical conductivity at elevated pressures. In: Poromechanics V – Fifth Biot Conference on Poromechanics. ASCE, Vienna, pp. 1415–1424.
- Mitchell, J., Sederman, A.J., Fordham, E.J., Johns, M.L., Gladden, L.F., 2008. A rapid measurement of flow propagators in porous rocks. *J. Magn. Reson.* 191, 267–272.
- Mutterlose, J., Bornemann, A., 2000. Distribution and facies patterns of Lower Cretaceous sediments in northern Germany: a review. *Cretac. Res.* 21, 733–759. <http://dx.doi.org/10.1006/cres.2000.0232>.
- Nguyen, Q.P., Rossen, W.R., Zitha, P.L.J., Currie, P.K., 2009. Determination of gas trapping with foam using X-ray computed tomography and effluent analysis. *SPE J. Soc. Pet. Eng.* 14, 222–236. <http://dx.doi.org/10.2118/94764-pa>.
- Olafuyi, O.A., Cinar, Y., Knackstedt, M.A., Pinczewski, W.V., 2011. Downscaled capillary pressure and relative permeability of small cores for network model validation. *Int. J. Eng. Res. Afr.* 4, 15–26 doi:10.4028. [www.scientific.net/JERA.4.15](http://www.scientific.net/JERA.4.15).
- Ramstad, T., Oren, P.E., Bakke, S., 2010. Simulation of two-phase flow in reservoir rocks using a Lattice Boltzmann method. *SPE J.* 15, 923–933. <http://dx.doi.org/10.2118/124617-pa>.
- Reichenbach-Klinke, R., Stavland, A., Langlotz, B., Wenzke, B., Brodt, G., 2013. New insights into the mechanism of mobility reduction by associative type copolymers. In: Paper presented at the SPE Enhanced Oil Recovery Conference, Kuala Lumpur, Malaysia, July 2–4, 2013.
- Reinicke, A., 2009. Mechanical and Hydraulic Aspects of Rock-proppant Systems Laboratory Experiments and Modelling Approaches (Dissertation). Deutsches GeoForschungZentrum, Potsdam, Germany.
- Reyer, D., Philipp, S.L., 2014. Empirical relations of rock properties of outcrop and core samples from the Northwest German Basin for geothermal drilling. *Geotherm. Energy Sci.* 2, 21–37.
- Romanenko, K., Balcom, B.J., 2013. An assessment of non-wetting phase relative permeability in water-wet sandstones based on quantitative MRI of capillary end effects. *J. Pet. Sci. Eng.* 110, 225–231. <http://dx.doi.org/10.1016/j.petrol.2013.08.025>.
- Ruedrich, J., Siegesmund, S., 2007. Salt and ice crystallisation in porous sandstones. *Environ. Geol.* 52, 225–249. <http://dx.doi.org/10.1007/s00254-006-0585-6>.
- Russ, J.C., Dehoff, R.T., 1991. Practical Stereology. Plenum Press, New York and London.
- Ruzyla, K., 1986. Characterization of Pore Space by Quantitative Image Analysis. <http://dx.doi.org/10.2118/13133-pa>. SPE-13133-PA.
- Selley, R.C., 2000. Applied Sedimentology. Academic Press, San Diego, California, United States.
- Shaw, J.C., Churcher, P.L., Hawkins, B.F., 1991. The Effect of Firing on Berea Sandstone. <http://dx.doi.org/10.2118/18463-pa>. SPE-18463-PA 6:72–78.
- Sheppard, S., Mantle, M.D., Sederman, A.J., Johns, M.L., Gladden, L.F., 2003. Magnetic resonance imaging study of complex fluid flow in porous media: flow patterns and quantitative saturation profiling of amphiphilic fracturing fluid displacement in sandstone cores. *Magn. Reson. Imag.* 21, 365–367. [http://dx.doi.org/10.1016/s0730-725x\(03\)00140-1](http://dx.doi.org/10.1016/s0730-725x(03)00140-1).
- Shojaikaveh, N., Berentsen, C., Rudolph-Floter, S.E.J., Wolf, K.H., Rossen, W.R., 2012. Wettability determination by equilibrium contact angle measurements: reservoir rock – connate water system with injection of CO<sub>2</sub>. In: Paper presented at the SPE Eupec/EAGE Annual Conference, Copenhagen, Denmark, January, 1, 2012.
- Shojaikaveh, N., Rudolph, E.S.J., van Hemert, P., Rossen, W.R., Wolf, K.H., 2014. Wettability evaluation of a CO<sub>2</sub>/water/Bentheimer Sandstone system: contact angle, dissolution, and bubble size. *Energy Fuels* 28, 4002–4020. <http://dx.doi.org/10.1021/ef500034j>.
- Siggel, L., et al., 2012. A new class of viscoelastic surfactants for enhanced oil recovery. In: Paper presented at the PE Improved Oil Recovery Symposium, Tulsa, OK, USA, January, 1, 2012.
- Simjoo, M., Dong, Y., Andrianov, A., Talanana, M., Zitha, P.L.J., 2013. CT scan study of immiscible foam flow in porous media for enhancing oil recovery. *Ind. Eng. Chem. Res.* 52, 6221–6233. <http://dx.doi.org/10.1021/ie300603v>.
- Simon, D.E., McDaniel, B.W., Coon, R.M., 1976. Evaluation of fluid pH effects on low permeability sandstones. In: SPE Annual Fall Technical Conference and Exhibition, Louisiana, New Orleans, October 3–6, 1976.
- Sing, K.S.W., Everett, D.H., Haul, R.A.W., Moscou, L., Pierotti, R.A., Rouquerol, J., Siemieniewska, T., 2008. Reporting physisorption data for gas/solid systems. In: Handbook of Heterogeneous Catalysis. Pergamon Press, Great Britain. <http://dx.doi.org/10.1002/9783527610044.hetcat0065>.
- Skauge, A., Ormhaug, P.A., Gurholt, T., Vik, B., Bondino, I., Hamon, G., 2012. 2-D visualisation of unstable waterflood and polymer flood for displacement of heavy oil. In: Paper presented at the 18th SPE Improved Oil Recovery Symposium, Tulsa, OK, United States, April, 14–18, 2012.
- Smeets, M., Golombok, M., 2010. Application of shear induced structure materials for brine flooding in sandstone oil reservoirs. *J. Pet. Sci. Eng.* 72, 270–276. <http://dx.doi.org/10.1016/j.petrol.2010.03.027>.
- Smith, T., McKibbin, R., 2000. An investigation of boiling processes in hydrothermal eruptions. In: Paper presented at the World Geothermal Congress, Kyushu-Tokohu, Japan, May 28–June 10, 2000.
- Sneider, R.M., 1987. Practical Petrophysics for Exploration and Development: AAPG Education Dept. Short Course Notes (Houston, TX, October).
- Stadtler, A., 1998. Der Bentheimer Sandstein (Valangin, NW-Deutschland): eine paläologische und sequenzstratigraphische Analyse. Selbstverlag Institut für Geologie, Mineralogie und Geophysik der Ruhr-Universität, Bochum, Germany.
- Stanchits, S., Fortin, J., Gueguen, Y., Dresen, G., 2009. Initiation and propagation of compaction bands in dry and wet Bentheim Sandstone. In: Vinciguerra, S., Bernabé, Y. (Eds.), Rock Physics and Natural Hazards. Pageoph Topical Volumes. Birkhäuser Basel, Germany, pp. 846–868. [http://dx.doi.org/10.1007/978-3-0346-0122-1\\_6](http://dx.doi.org/10.1007/978-3-0346-0122-1_6).
- Swaid, I., Wilke, K., Kessel, D., 1997. Relative permeabilities and rheology of polymers in sandstone cores. *Rev. l'Inst. Fr. Pet.* 52, 263–265.
- Taugboel, K., Van Ly, T., Austad, T., 1995. Chemical flooding of oil reservoirs. 3. Dissociative surfactant-polymer interaction with a positive effect on oil recovery. *Coll. Surf. A Physicochem. Eng. Asp.* 103, 83–90. [http://dx.doi.org/10.1016/0927-7757\(95\)03233-4](http://dx.doi.org/10.1016/0927-7757(95)03233-4).
- Thovert, J.F., Adler, P.M., 2011. Grain reconstruction of porous media: application to a Bentheim Sandstone. *Phys. Rev. E Stat. Nonlinear Soft Matter Phys.* 83, 056116.
- Van Baaren, J.P., Vos, M.W., Heller, H.K.J., 1990. Selection of Outcrop Samples, vol. 1 (TU Delft, Delft, The Netherlands).
- Wever, D.A.Z., Picchioni, F., Broekhuis, A.A., 2013. Comblike polyacrylamides as flooding agent in enhanced oil recovery. *Ind. Eng. Chem. Res.* 52, 16352–16363. <http://dx.doi.org/10.1021/ie402526k>.
- Wicksell, S.D., 1925. The corpuscle problem. A mathematical study of a biometric problem. *Biometrika* 17, 84–99.
- Wolf, K.-H.A.A., Hettema, M.H.H., 1995. Petrophysical and Mineralogical Properties of Over-burden Rock and Coal, Part 2 (R), vol. 22.1.40/13.11. Delft University of Technology, Utrecht. <http://dx.doi.org/10.2118/129659-PA>.
- Wonham, J.P., Johnson, H.D., Mutterlose, J., Stadtler, A., Ruffell, A., 1997. Characterization of a shallow marine sandstone reservoir in a syn-rift setting: the Bentheim Sandstone Formation (Valanginian) of the Röhlermoor Field, Lower Saxony Basin, NW Germany. In: Paper presented at the GCSSEPM Foundation 18th Annual Research Conference Shallow Marine and Nonmarine Reservoirs, December 7–10, 1997.
- Wright, H.M.N., Roberts, J.J., Cashman, K.V., 2006. Permeability of anisotropic tube pumice: model calculations and measurements. *Geophys. Res. Lett.* 33, L17316.
- Xiao, D., Balcom, B.J., 2014. k-t acceleration in pure phase encode MRI to monitor dynamic flooding processes in rock core plugs. *J. Magn. Reson.* 243, 114–121. <http://dx.doi.org/10.1016/j.jmr.2014.04.006>.
- Zhou, Y., Helland, J.O., Hatzignatiou, D.G., 2012a. A dimensionless capillary pressure function for imbibition derived from pore-scale modelling in mixed-wet rock images. In: Paper presented at the 18th SPE Improved Oil Recovery Symposium, Tulsa, OK, United States, April, 14–18, 2012.
- Zhou, Y., Helland, J.O., Hatzignatiou, D.G., 2012b. Pore-scale modelling of water flooding in mixed-wet rock images: effects of initial saturation and wettability. In: Paper presented at the 18th SPE Improved Oil Recovery Symposium, Tulsa, OK, United States, April, 14–18, 2012.